# NMR Diffusion and Relaxation Studies on Surfactant Systems

Steven J. Seedhouse

Honors Thesis

Department of Chemistry

The State University of New York College at Brockport

This paper was submitted May 13, 2008 to the Thesis Committee of the Department of Chemistry and to the Honors Program at the State University of New York College at Brockport in completion of the thesis requirement specified in the guidelines for the College Honors Program, as well as for the Award of Honors in Chemistry.

We the undersigned have read this thesis and recommend the Award of Honors in Chemistry to Steve Seedhouse upon completion of all requirements of graduation.

_____ _____

**Markus M. Hoffmann, PhD** **Date**
**Thesis Advisor**

_____ _____

**Stephen A. Godleski, PhD** **Date**
**For the Thesis Committee**

_____ _____

**Thomas W. Kallen, PhD** **Date**
**For the Thesis Committee**

_____ _____

**Donna Kowal, PhD** **Date**
**Interim Director, Honors Program**

**ACKNOWLEDGEMENTS**

I am grateful to Dr. Markus Hoffmann for his guidance and advice throughout my research. Also I am appreciative of the effort Dr. Hoffmann gave in making suggestions and giving advice for improving the thesis.

I also thank Mr. Steven A. Wowchuk for his support and reassurance throughout the construction of the thesis. His help has been invaluable.

I give thanks to the Chemistry department at SUNY College at Brockport, as well as Rochester Midland Corporation for the opportunity they provided me for conducting research during Summer 2007.

Thank you to my thesis committee members Dr. Thomas W. Kallen and Dr. Stephen A. Godleski for reviewing the manuscript.

**Table of Contents**

## 1. Introduction

### 1.1 Surfactants

Surfactants (surface activating agents) are frequently used for industrial and domestic applications[1]. These applications include, but are not limited to soaps and detergents, a multi-billion dollar industry worldwide that includes both man-made and naturally occurring surfactants. In addition to their widespread use as cleaning agents, surfactants are also part of the markets for paints, food, and explosives, among others[10]. Needless to say, surfactants are everywhere, and it is their unique bilateral structure that makes them so versatile.

In general, surfactants are molecules containing both hydrophobic and hydrophilic regions. There are three categories of surfactants including nonionic, ionic, and zwitter ionic, but for this study we are only concerned with nonionic surfactants. For nonionic surfactants, each molecule has a polar head group and a non-polar hydrophobic carbon chain. This unique structure allows multiple surfactant molecules to aggregate in aqueous solutions to form micelles. The structure of a micelle is such that the long hydrophobic chains arrange themselves along the interior of the aggregate, with the polar head groups comprising the outer shell of the micelle. The hydrophobic nature of the interior of a micelle allows for the inclusion of similar hydrophobic organic compounds in the interior of the micelle. A sketch of the formation of typical micelles in water is shown in *Figure 1*.

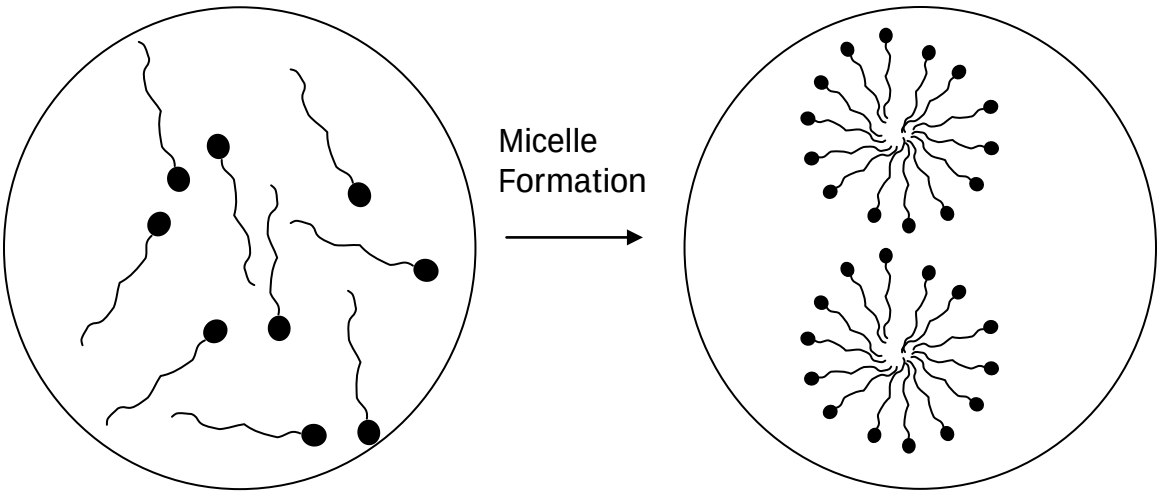


*Figure 1, Sketch of micelle formation in water*

In Figure 1, the surfactant molecules are shown as ball-and-stick models. The black, circular ends represent the polar head groups of the surfactant molecules, while the long thin tails represent the extended hydrocarbon chains. The circular representation of micelles in the right image in *Figure* 1 represents a cross section of a spherical micelle. While this typical model of a micelle appears spherical and rigid, with all of the hydrocarbon tails facing the interior of the micelle, it is important to note that this is not indicative of the complexity of micelle structure. The structural arrangement of a micelle is highly dynamic, with surfactant molecules shifting within an individual micelle, as well as leaving to join other micelles[2].

This structure is very favorable energetically because there are significant hydrophobic-hydrophobic interactions between the long carbon chains on the interior, dipole-dipole interactions between the polar head groups, and dipole-dipole interactions between the surrounding water molecules and the polar head groups of the surfactants.

The surfactant used in this study was a polydisperse branched alkyl-polyethoxy/propyloxy alcohol, so in a sample of this surfactant, molecules were of

varying polyethoxy chain lengths. The key structural elements of the most common form of this surfactant molecule include a branched alkyl chain containing a total of ten carbon atoms, followed by 7 repeating ethoxy units, 2 propyloxy units and a terminal hydroxyl group. The acronym C10E7P2OH was chosen to represent the surfactant in order to highlight the key structural features. *Figure 2* shows the structure of the surfactant C10E7P2OH with the most common polyethoxy chain length (7).

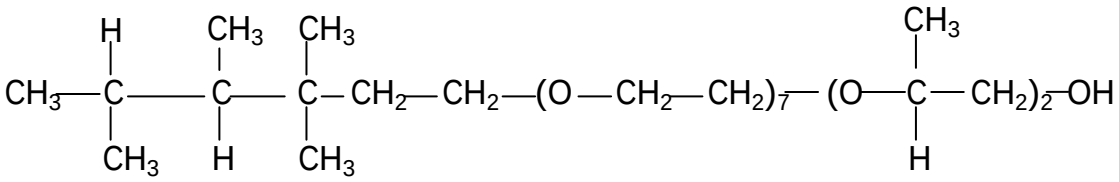

*Figure 2, Structure of C10E7P2OH Surfactant*

In aqueous solution the lowest energy place for an added foreign hydrophobic molecule to reside is on the interior of the surfactant micelles due to favorable hydrophobic-hydrophobic interactions. The foreign molecule must be sufficiently small to fit inside of the surfactant micelles. Also, the concentration of this foreign hydrophobic molecule must be sufficiently small so that all of the molecules can be contained inside of the micelles. If either of these conditions is not met, the foreign molecule will partition between inside the micelles and the bulk water solvent. Unfavorable hydrophobic-hydrophilic interactions will result until depending on its vapor pressure and concentration in solution, it either exits the solution by evaporating from the surface, or forms aggregates of its own in order to alleviate most of the unfavorable interactions. It is important to note that even for extremely hydrophobic compounds like D-limonene, there is still an equilibrium between its residence inside of micelles and within the bulk water

solvent. These hydrophobic compounds therefore still have a very small, but finite solubility in water.

In this study, D-limonene was introduced to C10E7P2OH/water solutions and compared with those solutions that contained only the surfactant C10E7P2OH and water. The structure of D-limonene is shown in *Figure 3.*

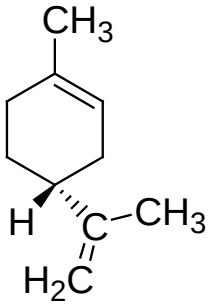


*Figure 3, Structure of D-limonene*

D-limonene's solubility in water is extremely low because it is very hydrophobic. We intended to determine the average radius of the surfactant aggregates in these solutions, as well as the aggregate number (the number of surfactant molecules comprising an average micelle). Also, we sought to answer the question, "Once D-limonene is introduced to the surfactant/water system, where does it associate?" These specific questions can be answered using data obtained from Nuclear Magnetic Resonance (NMR) spectroscopy of the surfactant systems. Specifically, $T_1$ relaxation, $T_2$ relaxation, and Diffusion-Ordered Spectroscopy (DOSY) are the experiments that provide data that help describe the molecular arrangement of surfactant micelles and association of D-limonene. This is an experimental approach that has been used previously by Kato[5] and Gerardino[1] among others.

The micelle arrangement was studied through comparison of measurements across a specific temperature range for three specific concentrations of surfactant in the presence and in the absence of D-limonene. The three surfactant concentrations were 2%, 3.5%, and 5% by mass of C10E7P2OH in water and the concentrations of D-limonene, when present, were fixed at 2% by mass. In total, six solutions were studied and compared across a specific temperature range.

**1.2 NMR Spectroscopy**

Some nuclei possess a property called spin which is observed in NMR Spectroscopy. These spin-bearing nuclei are precessing at a specific Larmor frequency which creates a magnetic vector pointing perpendicular to the plane of the rotational motion. A superconducting electromagnet, the crucial part of an NMR instrument, applies a large external magnetic field to the sample, which forces the magnetic vector of each precessing nucleus (spin) in the sample to align along the external magnetic field. The magnetic moments of each nucleus point either with or against the direction of the magnetic field. More then 50% of the spins align with the external magnetic field, thereby creating a net vector which is termed the bulk magnetization. *Figure 4* illustrates this alignment process within the NMR instrument.

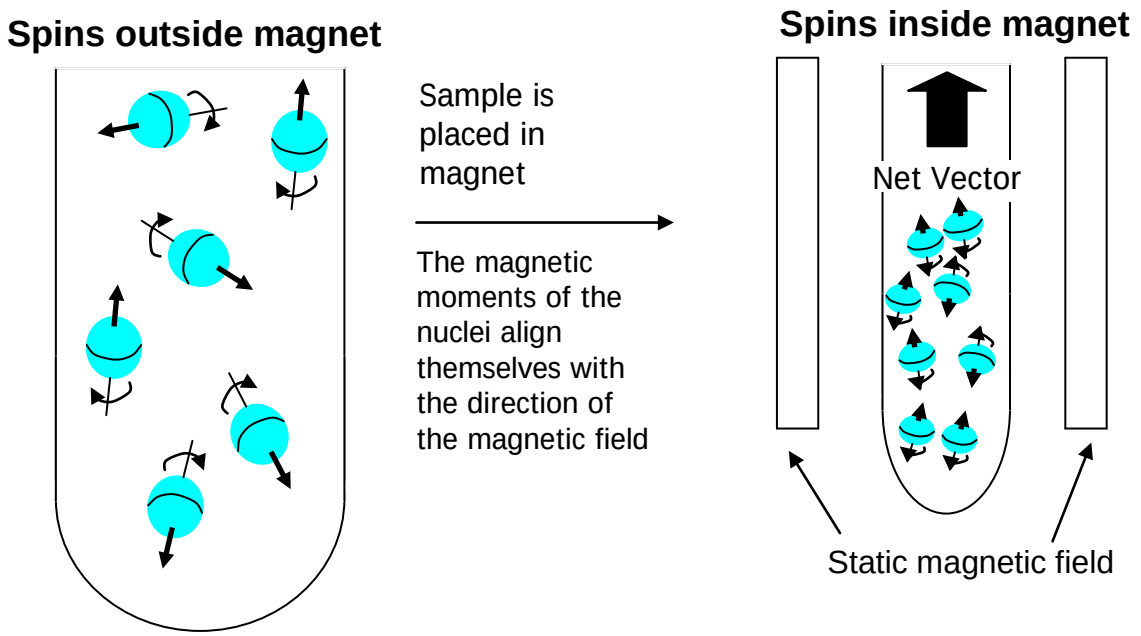


*Figure 4, The effect of the magnetic field on the magnetic vectors of the nuclei in a sample*

The nuclei are represented in *Figure 4* by showing their rotation as well as the magnetic moment vector, indicated by the black arrow perpendicular to the plane of their rotation. In a sample tube outside of the magnet, the nuclei align randomly as shown on the left of *Figure 4*. Within the static magnetic field of the NMR instrument, the magnetic moments align vertically and the net vector in the upward direction is established[3], as shown on the right of *Figure 4*.

### 1.3 $T_1$ and $T_2$ Relaxation

One can manipulate the net vector, also referred to as bulk magnetization, by introducing magnetic radio frequency (rf) pulses. The rf pulse is caused by a second external magnetic field perpendicular to the static magnetic field which is created by a coil within the instrument and functions to tilt the bulk magnetization vector from its resting axis. The longer the magnetic pulse is maintained, the further the net vector of the

bulk magnetization is moved. A longer pulse therefore causes the bulk magnetization to shift further from the z-axis.

Because each of the nuclei are rotating with their magnetic moments aligned along the z-axis, when the bulk magnetization is tilted from the z-axis by a pulse, the relaxation that follows is very complex because each magnetic moment is precessing around the z-axis while relaxing. This complex motion is best analyzed in the "rotating frame" coordinate system. The rotating frame is a coordinate system which helps to better visualize the relaxation that occurs after an rf-pulse within the NMR instrument. The coordinate system of the rotating frame rotates with the nucleus so that the only motion observed is the relaxation towards the z-axis[3].

An illustrative analogy to the rotating frame is the motion of a carousel. Two simultaneous motions are occurring on a carousel: the rotation of the entire carousel, as well as the up and down motion of each individual horse on the carousel. To an observer on the ground who was tracking the motion of one particular horse, the motion would be very complex and hard to visualize. If the same observer were to stand on the carousel as it rotated and then observe a particular horse, the motion would only appear as a simple up-down oscillation. This concept is identical to the rotating frame coordinate system applied to the relaxation of each nucleus[3]. An example of a 90º pulse within the rotating frame coordinate system is shown in *Figure 5*.

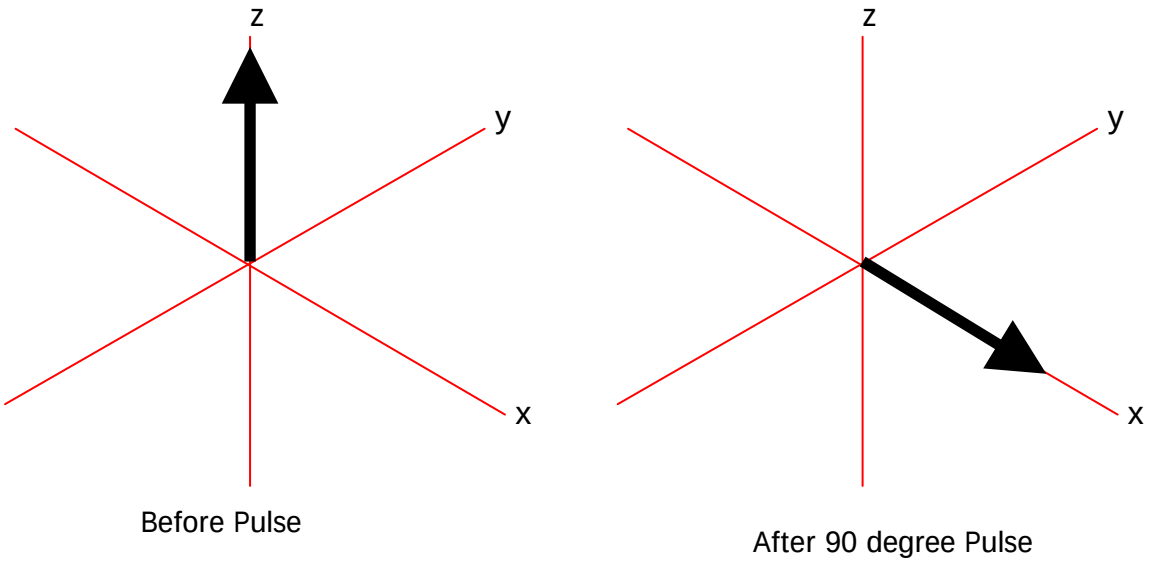


*Figure 5, 90º rf-pulse*

The bulk magnetization is represented in *Figure 5* by the thick black arrow within the rotating frame coordinate system, which is aligned with the z-axis before the rf-pulse is introduced. During the rf-pulse the bulk magnetization is rotated away from the z-axis and in the case of a 90 degree y-pulse brought along the x-axis, i.e., into the x-y plane, as shown on the right in *Figure* 5. Once the pulse is released, the bulk magnetization is actually allowed to relax in two distinct ways. $T_1$ relaxation is characterized by the bulk magnetization relaxing back towards the z-axis, that is, back to its original orientation. $T_2$ relaxation occurs within the xy-plane. In $T_2$ relaxation, the individual magnetic moments separate across the xy-plane. Each type of relaxation can be measured and a time constant describing the rate of this relaxation can be determined for each using experiments described in Section 1.6.

### 1.4 Detection

After an rf-pulse has been introduced and the bulk magnetization begins to relax, the same coil that delivered the magnetic pulse then becomes the antenna for detection. The precessional magnetization that was created induces a current in the same coil that was used to introduce the rf-pulse. This coil, now acting as an antenna, detects a current, which is recorded as the free induction decay (FID). Because the vector is rotating while it is relaxing to the z-axis, the radius that the magnetic vector carves becomes smaller as the vector nears its resting position on the z-axis. The decreased radius is observed as the fading oscillatory signal, i.e., the FID[3]. A typical FID is shown in *Figure 6*.

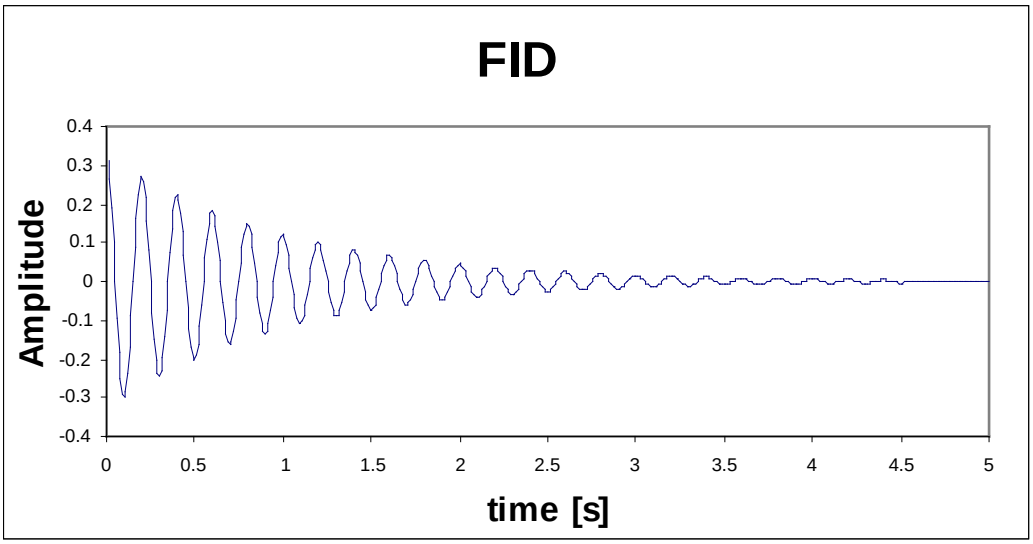


*Figure 6, Example of a typical FID*

*Figure 6* shows the decay of the signal over time due to spreading of the net vectors in the xy plane and also due to inhomogeneity in the magnetic field within the NMR instrument.

### 1.5 Fourier Transformation

The FID is the raw data collected from the NMR instrument. The Fourier transformation is a mathematical operation which allows one to convert the FID into a more readable spectrum. The method of the Fourier transformation begins by multiplying trial cosine waves of many different frequencies with the FID. At each frequency, a unique product function is obtained. This operation is applied to the very same FID data for all frequencies specified by the frequency spectral width and resolution parameters of the NMR experiment. The operation is shown at three different frequencies in *Figure 7.*

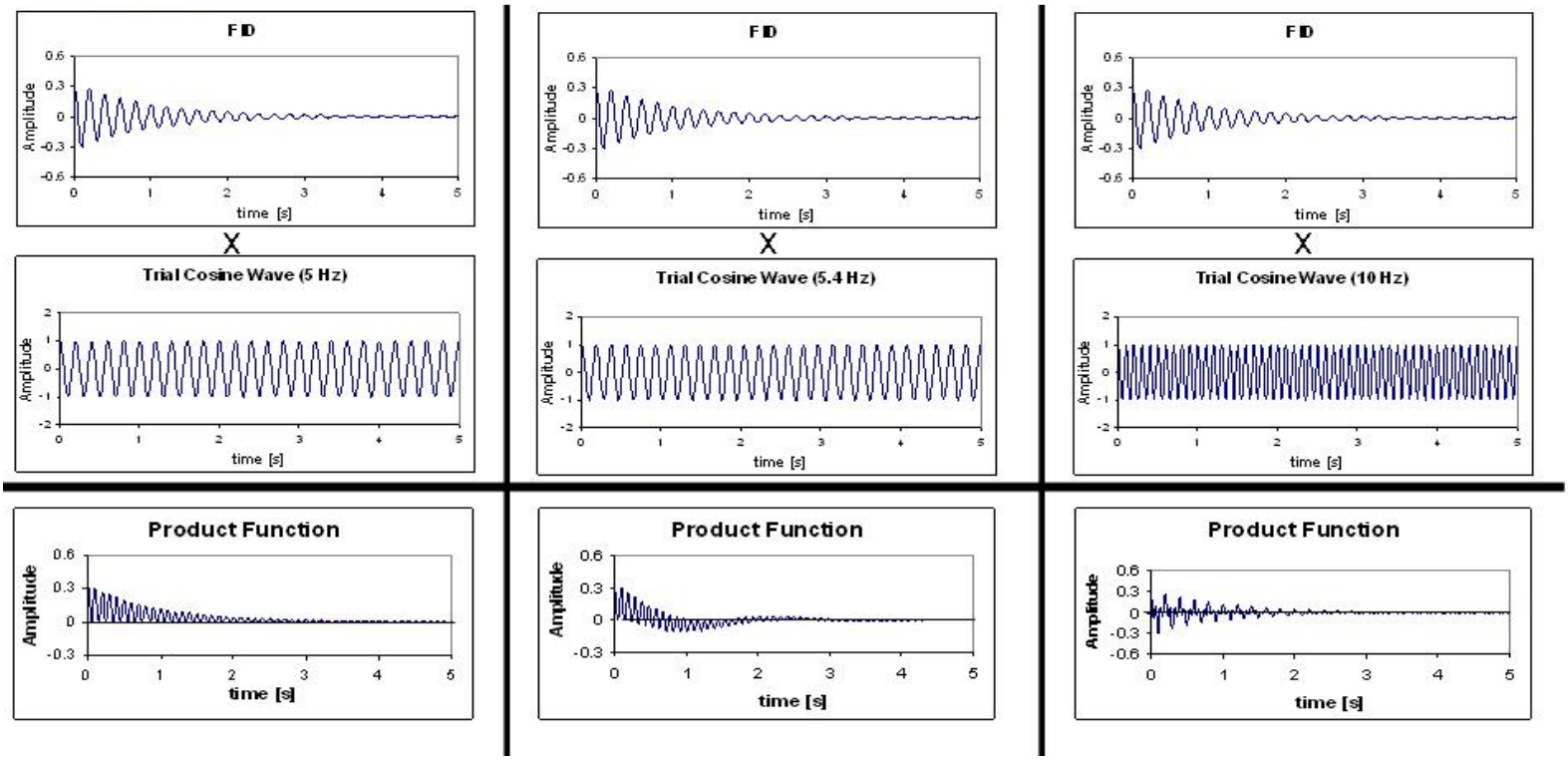


*Figure 7, Fourier transformation*

*Figure 7* shows three different trial functions, all of differing frequencies being multiplied by the FID for a random experiment. Along the bottom row are the product

functions that result from each of the three combinations. Note that the same FID is used for each operation and the varying frequencies of the trial cosine wave functions are what determine the variation in the product functions[3].

Once this operation has been performed at every frequency specified by the parameters of the experiment, the product functions are integrated and the resultant values are plotted against the frequency of the trial cosine wave that was used to create that product function. This conversion is illustrated in *Figure 8*.

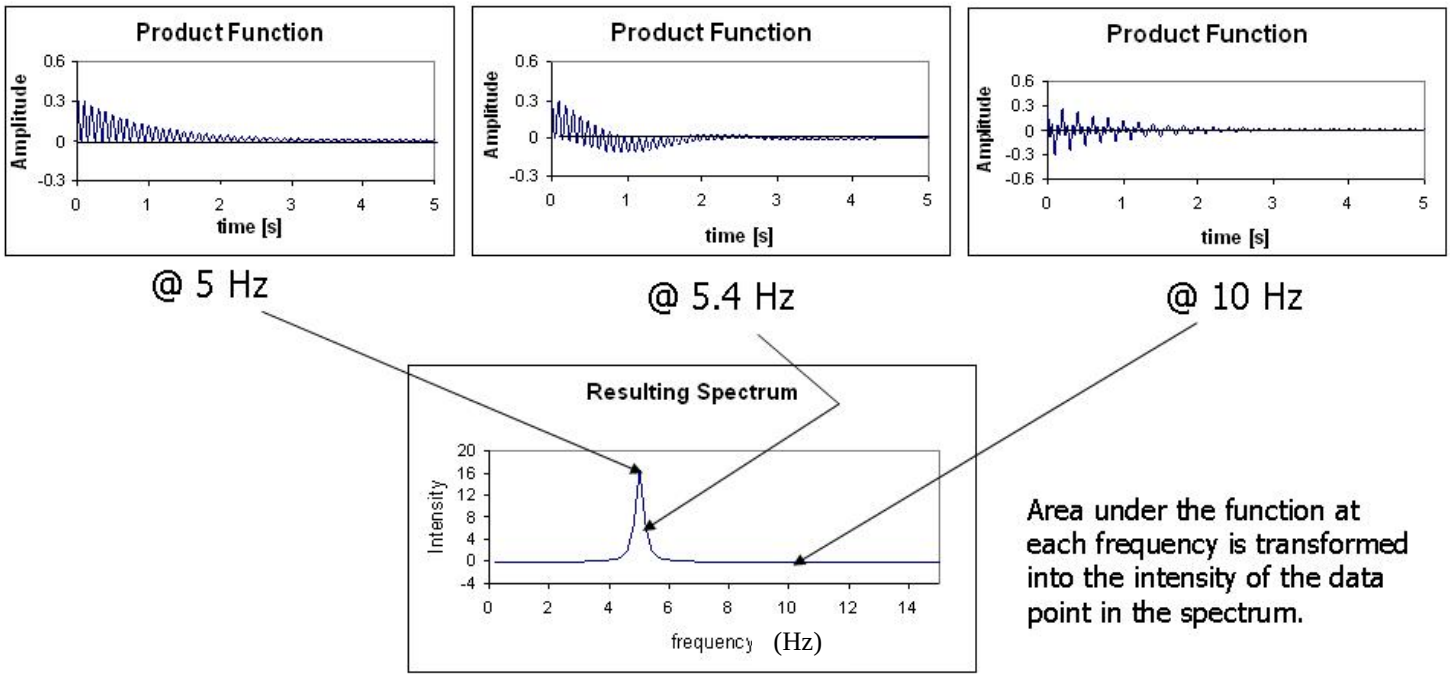


*Figure 8, Conversion of the product functions to the final spectrum*

*Figure 8* shows the integration of the product functions and the resulting spectrum. These are just three examples of product functions obtained from a series of operations that would include trial functions of frequencies spanning the entire range 0-15 Hz for this experiment.

The Fourier transformation is useful in many spectroscopic applications to obtain a spectrum that is more easily interpreted than the time-domain function (FID).

### 1.6 Advanced NMR Experiments

For this study, a series of more complex NMR experiments were used to obtain useful information about the surfactant systems. These experiments rely upon all of the concepts already introduced. The three experiments that were used in this study are inversion-recovery for obtaining $T_1$ time constants, CPMG (named for its inventors Carr, Purcell, Meiboom, and Gill) for obtaining $T_2$ time constants, and diffusion measurements for obtaining the diffusion coefficient, *D*, of the aggregates.

#### 1.6a Determining $T_1$ Time Constant

The inversion-recovery program allows for measurement of the $T_1$ time constant for the nuclei in the sample. It begins with a specific time period during which the bulk magnetization is allowed to settle to its resting position along the z-axis. The program then introduces a 180º pulse to invert the bulk magnetization. This pulse is followed by a variable delay time during which the bulk magnetization relaxes back towards the z-axis by $T_1$ relaxation. Next, the program introduces a 90º pulse to inspect how far the magnetization has relaxed back and then the detection of the FID begins. This standard pulse program is illustrated in *Figure 9.*

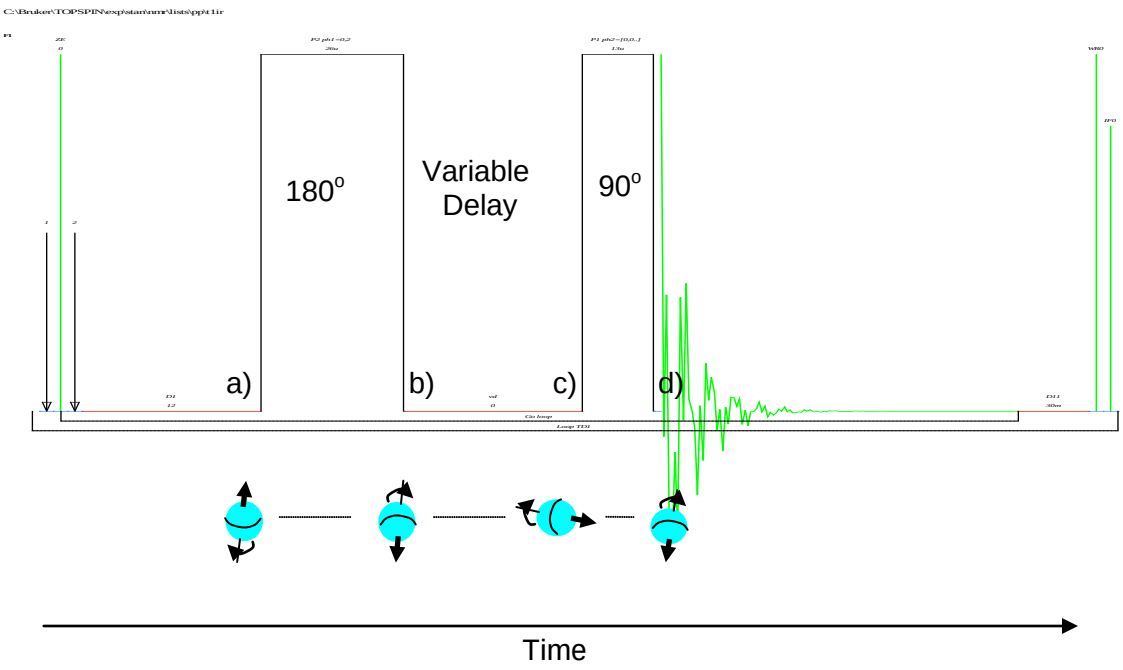


*Figure 9, standard pulse program*

At point "a" in *Figure 9*, the bulk magnetization is aligned along the z-axis. The 180° pulse, shown as a rectangle, rotates the bulk magnetization away from the axis as shown by the nuclei across the time axis at point "b." During the variable delay time between point "b" and "c," $T_1$ relaxation occurs. The final 90° pulse moves the bulk magnetization again. The FID is read and recorded beginning at point "d." This FID is shown in the background to the pulse program in *Figure 9*. This sequence is repeated 16 times, each with a different delay time between points "b" and "c," as designated in the pulse program parameters. Each of the 16 FID corresponding to each variable delay time is Fourier transformed and phased using identical phase settings to yield readable, phased spectra, also termed slices. For each signal of interest, the area under the signal is integrated and the integrated values for each peak, also referred to as the magnetizations, are plotted against the corresponding delay time. This plot, shown on the right in *Figure*

10 can be fitted to yield the relaxation rate $1/T_1$ which allows the derivation of the rate at which the bulk magnetization relaxes ($T_1$ time constant). This rate is unique for every nucleus type. A waterfall plot of the 16 $T_1$ slices and the associated Inversion Recovery plot are shown in *Figure 10.*

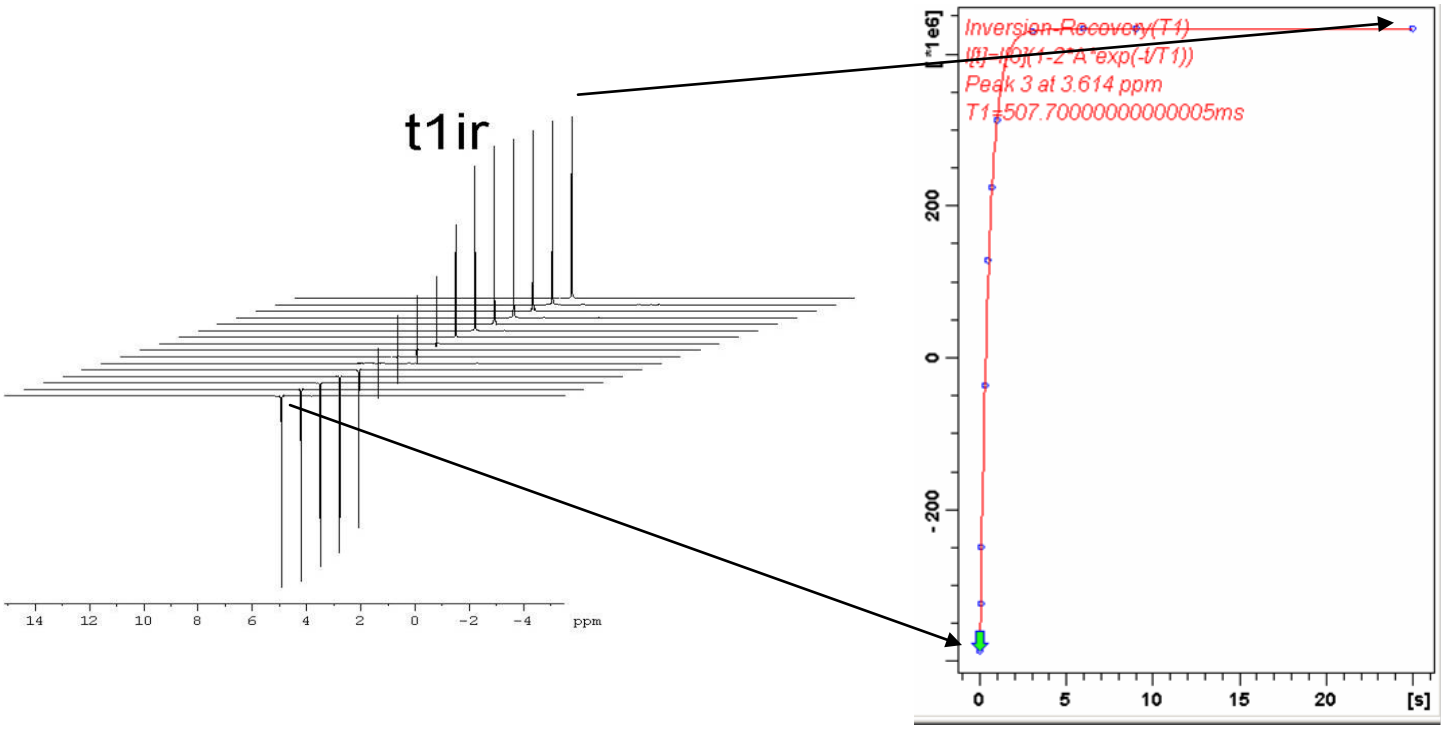


*Figure 10, $T_1$ slices and $T_1$ time constant plot*

*Figure 10* shows the sixteen slices for a sample of pure water on the left arranged in a waterfall plot. Arrows are shown to relate the 1st and 16th slices with their corresponding data points along the curve on the right for magnetization vs. delay time. The number of slices, or delay times, that are to be taken is variable. For this study sixteen was an optimal number, given the desired precision and time constraints for the instrument.

### 1.6b Spin Echo

Spin Echo is a phenomenon that occurs following a 90º rf pulse, which tilts the bulk magnetization onto the xy plane, and a 180º rf pulse, which reverses the polarity of the magnet and direction of spread in the xy plane. The spin echo results from the refocusing of the magnetic vectors after the polarity of the magnetic field in the NMR instrument is reversed. Following a pulse, the vectors begin to relax according to their $T_2$ relaxation constants. This relaxation causes the vectors to spread across the xy-plane as described in section 1.3. An additional contributor to this spread across the xy-plane is inhomogeneity in the magnetic field. In order to remove this contribution to $T_2$ and determine what portion of the spread is due only to $T_2$ relaxation, after a certain time, $\tau$, a 180º inversion pulse is introduced which reverses the direction of spread due to the magnet inhomogeneity. As the magnetic vectors refocus, the FID essentially reappears after another identical time period, $\tau$. Because of the virtual reappearance of the FID showing the spin-spin relaxation, the phenomenon is termed spin echo[3]. This phenomenon is observed in the $T_2$ experiment described in section 1.6c.

### 1.6c Determining $T_2$ Time Constant

The standard pulse program used to determine the $T_2$ time constant is slightly more complex then the standard pulse program for determining $T_1$ constants. Initially, a 90º pulse is applied to align the bulk magnetization in the xy-plane. There is a specific time period, $\tau$, following the initial 90º pulse during which $T_2$ relaxation occurs, causing the individual magnetic vectors to spread across the xy-plane. During this time, $\tau$, inhomogeneity in the magnetic field inside the NMR instrument also contributes to this

spread, as previously described. In order to remove this coherent contribution to the spread, a 180º pulse in the xy-plane is then applied to reverse the magnet polarity. After an identical time period, $\tau$, the spread due to magnetic field inhomogeneity refocuses and the spin echo is formed. The remaining spread of the magnetic vectors across the xy-plane is due only to the random $T_2$ relaxation process that has occurred during the $2\tau$ time period. This sequence is illustrated in *Figure 11*.

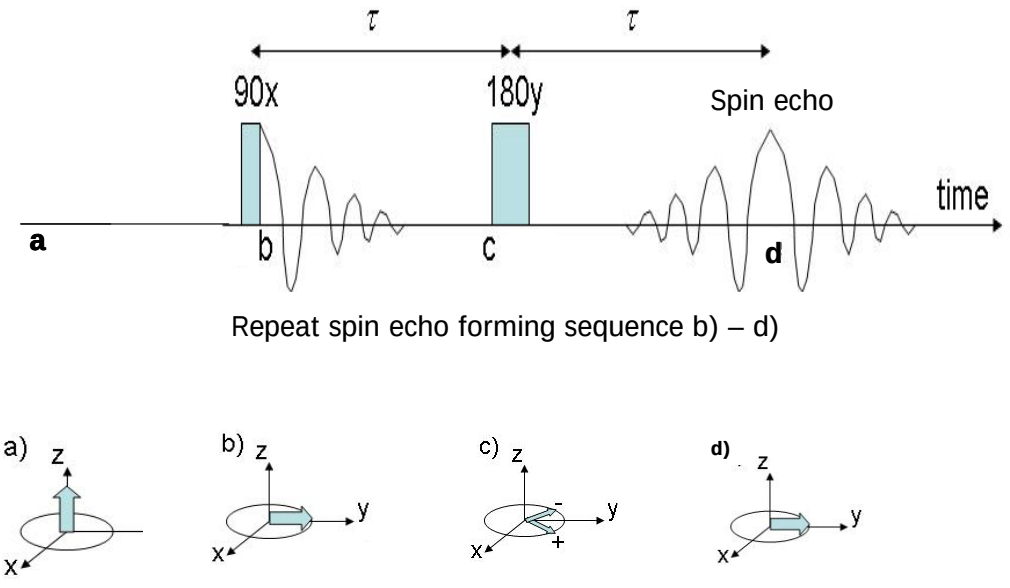


*Figure 11, $T_2$ standard pulse program*

*Figure* 11 shows the bulk magnetization initially aligned with the z-axis at point "a." At point "b," a 90º pulse is introduced, which aligns the magnetic vectors in the xy-plane. The individual magnetic vectors spread along the xy-plane between point "b" and point "c" due to inhomogeneity in the NMR magnet and also due to $T_2$ relaxation. At point "c," a 180º pulse is introduced to reverse the magnet polarity. By point "d," the remaining spread of the vectors in the xy-plane is due only to $T_2$ relaxation. The spin echo forming sequence ("b" to "d") is repeated a variable amount of times and the net

vector is measured and recorded as one slice, which becomes one data point for a plot of spin echo intensity vs. total time of the n times Tau – 180º pulse – Tau sequence, which is then fitted to determine the $T_2$ time constant. When more spin echo sequences occur, there is more spread due to $T_2$ relaxation because more time is given for the relaxation to proceed. Therefore, the resultant net vector will be of decreasing magnitude when more spin echo sequences are repeated. For each successive slice, the number of spin echo sequences ("b"-"d") is increased in this way. An example of the sixteen slices after they have been Fourier transformed and phased with identical phase settings, and their associated plot to determine $T_2$ are shown in *Figure 12*.

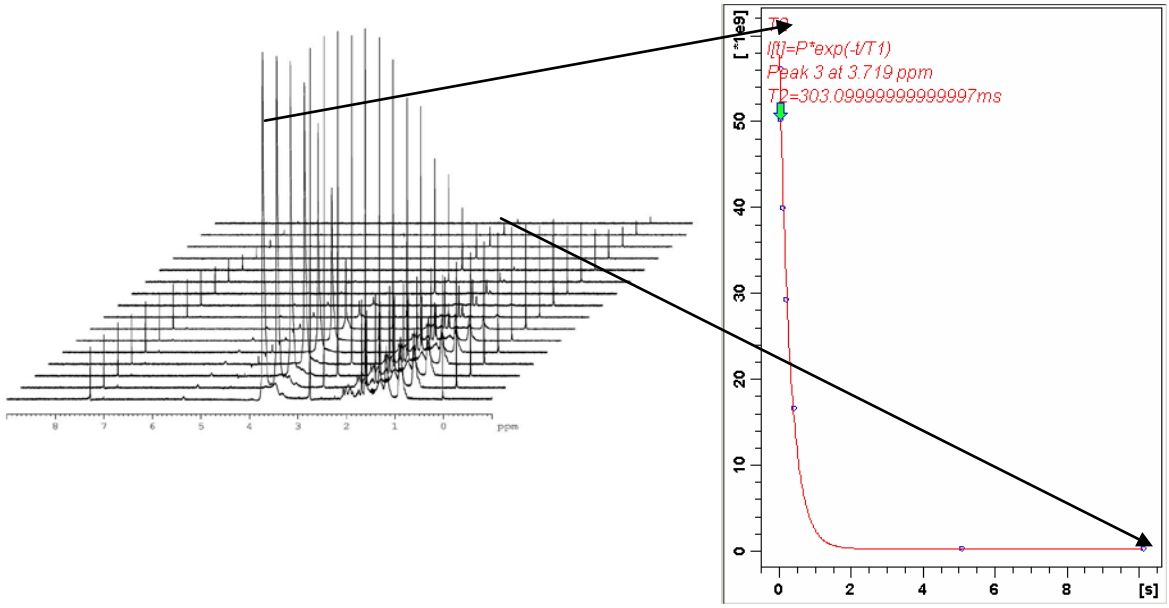


*Figure 12, $T_2$ slices and their associated plot*

In this figure, the $T_2$ slices for a sample of C10E7P2OH in water with D-limonene are arranged in a waterfall plot on the left. Each individual signal in the spectra can be integrated across all sixteen slices to yield a $T_2$ value specific to that peak. Arrows are used to correlate the first and sixteenth slice, with the corresponding integration value

plotted against the number of spin echo sequences for that slice, for the largest surfactant signal. The significance of the ability to integrate any number of peaks is further described in Section 2.5.

### 1.7 Diffusion-Ordered Spectroscopy (DOSY)

The fundamental difference between standard NMR experiments including $T_1$ and $T_2$, and DOSY is the presence of a magnetic field gradient during a DOSY experiment. In $T_1$ and $T_2$ experiments, the magnetic field is of uniform strength. Positions within the sample tube can be differentiated based upon their position in the gradient and the movement (diffusion) of individual molecules within the solution can be tracked. Based on these principle ideas, the NMR instrument can determine diffusion coefficients for the different molecules present in a solution.

The pulse program for DOSY is principally based upon the same general spin echo sequence shown in *Figure 12*, but is further refined to optimize the accuracy of diffusion measurements by eliminating sources of error such as eddy currents and convection currents caused by gradient pulses. The pulse program for obtaining diffusion coefficient, *D*, was even slightly more complex, as pulsed field gradients were used in place of static field gradients. However, the effect of the magnetic field gradient manifests itself in the bulk magnetization after the $\tau - 180^o - \tau$ time length. For example, nuclei that reside in a strong part of the gradient at the beginning of the pulse sequence will experience a lot of spread along the xy-plane of their magnetic moments. If these nuclei diffuse to a position of weaker magnetic field strength within the gradient after the $180^o$ pulse, which reverses the direction of spread of the magnetic vectors, then they will

not be allowed to refocus completely. For the experiments in this study, a total of sixteen different field gradient strengths were applied, and the resultant FID is obtained from each sequence using the different gradient field strengths. A stronger field gradient will yield a weaker spin echo. For DOSY, these sixteen trials provide, after Fourier transformation of the spin echo and consistent phasing, the resulting sixteen spectra. Any signal can be integrated across all sixteen slices and used to determine *D* for the molecule that is represented by that signal. An example of such a plot is shown in *Figure 13.*

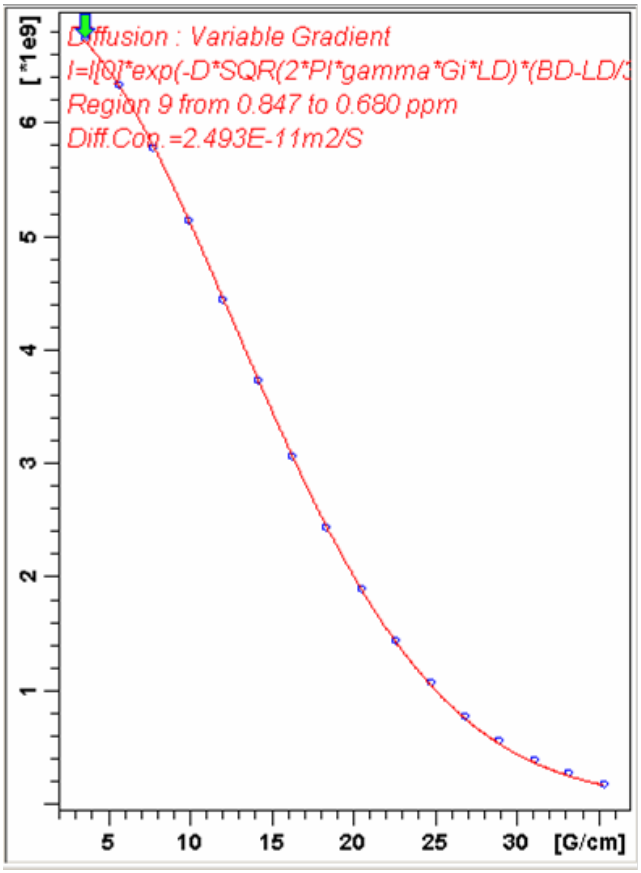


*Figure 13, Plot for determining D from 16 slices in a DOSY experiment*

The equation of fit for this plot is *Equation 1*,

$$I = I_o e^{-D\gamma^2 g^2 \delta^2 (\Delta - \delta/3)} \quad (1)$$

where $I$ is the observed intensity (arbitrary units), $I_o$ is the reference intensity (arbitrary units), $D$ is the diffusion coefficient ($m^2/s$), $\gamma$ is the gyromagnetic ratio (Hz/G), $g$ is the amplitude of the applied gradient (G/m), $\delta$ is the duration of the applied gradient (s), and $\Delta$ is the diffusion time (s). All of the factors in this equation are known and declared in the parameter set for the pulse program except $I_o$, and $D$, which is determined from the fit. *Equation 1* can be rearranged to show that the observed intensity units are indeed irrelevant:

$$\frac{I}{I_o} = e^{-D\gamma^2 g^2 \delta^2 (\Delta - \delta/3)} \qquad (2)$$

In this form, it is obvious that the observed and relative intensities cancel making their units irrelevant.

It is clear from *Equation 2* that there is a dependency of the intensity of the signal integration, $I$, on the magnetic field gradient, $g$. Therefore, by altering the gradient field strength across sixteen spectra, the plot shown in *Figure 13* can be obtained and fitted to *Equation 1* in order to determine the diffusion coefficient.

**1.8 Theory on Diffusion**

Determining $D$ is important for examining the structure and activity on a molecular level of surfactant aggregates in solution. By assuming spherical micelles, one can calculate the surfactant aggregate radius using the Stokes-Einstein Equation[7], *Equation 3*.

$$r = \frac{kT}{6\pi\eta D} \qquad (3)$$

In *Equation 3*, $r$ is the aggregate radius (m), $k$ is the Boltzmann constant ($1.380 \times 10^{-23}$ J/K), $T$ is temperature (K), $\eta$ is viscosity of the solution (Pa*s), and $D$ is the diffusion coefficient ($m^2/s$). The Stokes-Einstein equation, *Equation 3*, is limited for use only as it applies to media of high fluidity, where the diffusing particle is a large entity moving through a continuous medium, as is the case in this study.

In order to determine if the foreign fragrance molecule D-limonene associates either within or outside these aggregates, one can compare the values of $D$ in each sample. For instance, if $D$ is significantly different for each species, then it is evident that the two molecule types do not migrate together in solution. This would eliminate the possibility of mixed aggregates forming which include both surfactant and D-limonene. Similar $D$ values for each molecule would indicate that they are probably diffusing as one entity in the solution, confirming the presence of mixed aggregates.

In addition to this analysis, $T_1$ relaxation and $T_2$ relaxation experiments can also yield information regarding the environment of the aggregates in solution. Comparisons of $T_1$ and $T_2$ relaxation values can describe whether the entity is large (> 500 FM), and therefore within the spin-diffusion limit, or small (FM < 500), and therefore described by the extreme narrowing limit (where T1= T2)[9]. For larger entities described by the spin-diffusion limit, there is magnetic shielding of nuclei in any cluttered molecular environment, called the chemical shift anisotropy (CSA). At sufficiently high external magnetic field strength, this shielding leads to fluctuating magnetic fields because the CSA depends upon the orientation of the molecule in the external field, which is dynamic[8]. These fluctuations influence the relaxations of the nuclei, causing $T_1$ and $T_2$ to

be unequal. Therefore, if $T_1$ and $T_2$ values are significantly different for the same component, their difference is evidence of an environment described by the spin-diffusion limit. Large aggregates, as opposed to individual small molecules, are present.

## 2. Results and Discussion

### 2.1 Phase Behavior

There is an optimal range of temperatures in which reliable NMR experiments can be conducted for the surfactant systems we have studied,. In solutions of C10E7P2OH in water, there is a phase change from a single-phase, clear solution to a cloudy two-phase system beyond a certain temperature. This phenomenon exists because at low temperatures and high concentrations, surfactant micelle formation is favored and therefore a single-phase, clear solution results. As an individual, unassociated molecule though, C10E7P2OH is not very soluble in water because it is nonionic and has a long hydrophobic carbon tail. As temperature increases then, there is enough thermal energy to break apart the surfactant micelles and segregate the surfactant in solution into a separate, surfactant-rich phase[12]. Experimentally, the double-phase cloudy solutions yield bizarre, unreadable spectra when analyzed in the NMR spectrometer, so it is essential to determine the temperature range at which the solutions were always clear and single-phased. The data for this phase behavior investigation are shown in *Figure 14.*

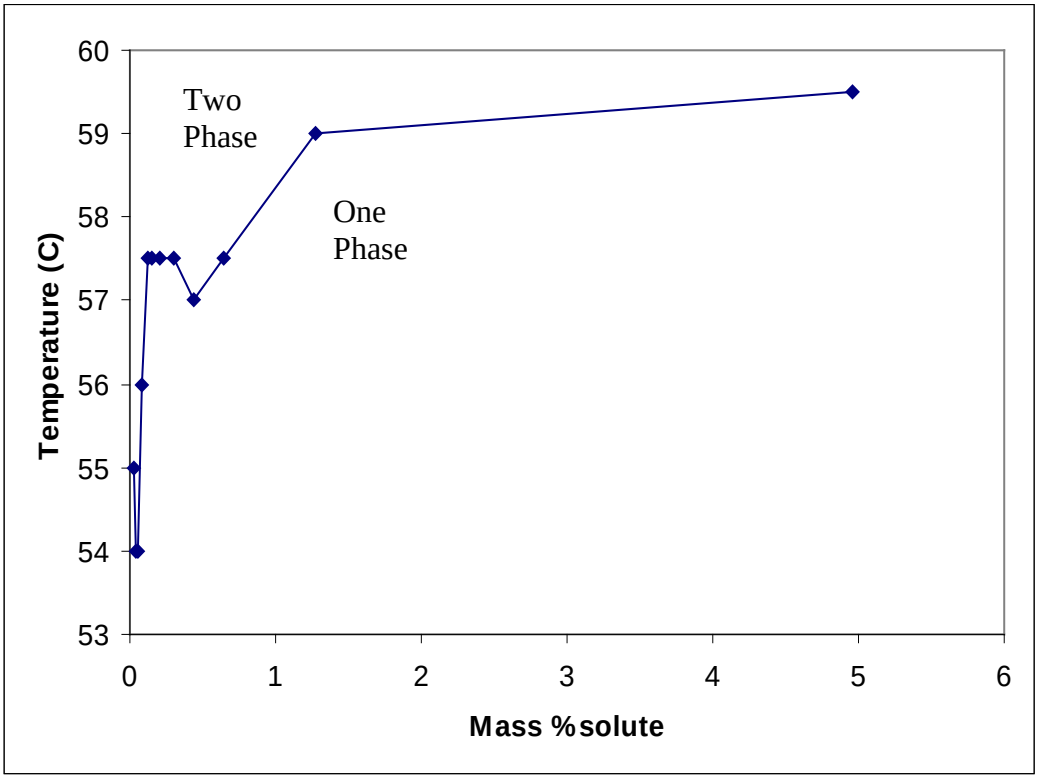


*Figure 14, Phase behavior of C10E7P2OH solutions*

The two-phase state exists above the curve and the one phase state below the curve. *Figure 14* shows that the cloud point temperatures for the composition range 2% to 5% by mass C10E7P2OH in water used for the NMR studies are between approximately 50-60º Celsius. Mixtures containing only 2-5% by mass D-limonene and water are cloudy at room temperature because D-limonene is completely hydrophobic and therefore the mixture is bi-phasic. For solutions containing C10E7P2OH and D-limonene in water, the cloud point is observed around 35º Celsius using identical surfactant concentrations, with 2% by mass D-limonene added. The presence of the surfactant aggregates in these solutions allows the D-limonene to be incorporated within the micelles and a single-phase state is maintained below 35º Celsius. However, beyond this temperature there is enough thermal energy again to cause a break-up of the

aggregate and a change to two phases. The existence of a single-phase state below the cloud point is also corroborated by the NMR spectra obtained at these temperatures. These spectra were normal and yielded good, observable data.

The temperature range for the NMR experiments is reflective of the phase behavior study. Because of the lower cloud point temperature of solutions containing D-limonene, NMR spectra were only obtained at temperatures of 308K and below.

**2.2 Viscosity**

In order to determine the aggregate number for C10E7P2OH in the surfactant systems of interest using the Stokes-Einstein equation of *Equation 2*, it was necessary to also determine the viscosities of each solution at the various temperatures of the study. The data for the viscosities are shown in *Figure 15*.

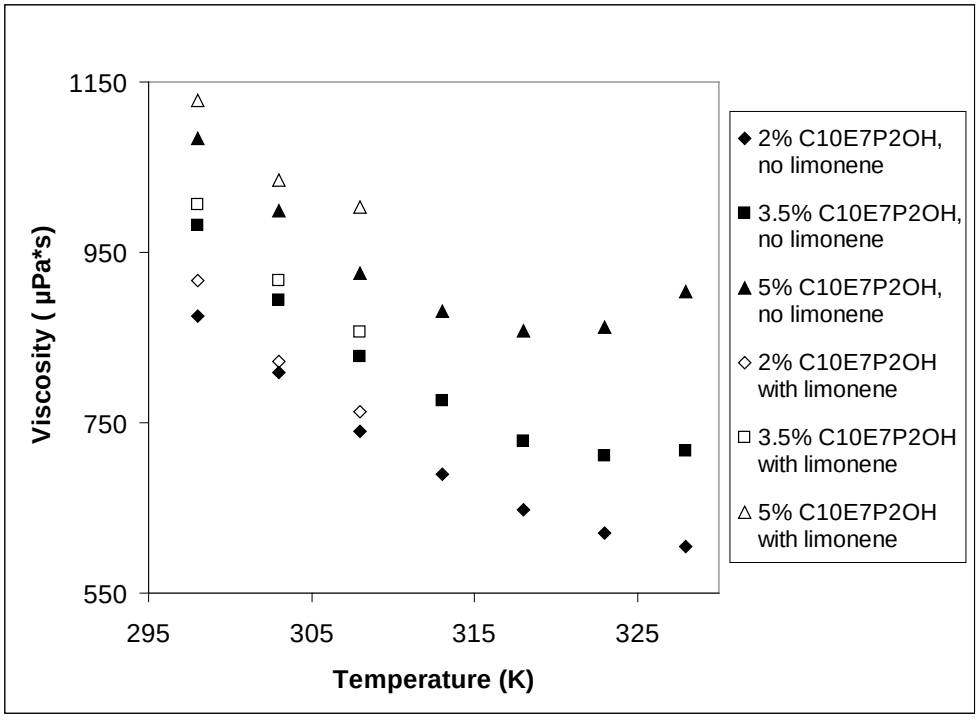


*Figure 15, Viscosity of C10E7P2OH solutions at various temperatures*

In *Figure 15*, viscosity is plotted along the y-axis and Temperature along the x-axis. The data for the solutions containing D-limonene are shown in white with black outline and the solutions without D-limonene in solid black. Viscosity decreases with temperature for all of the solutions between 298 Kelvin and 318 Kelvin. This behavior is expected because as temperature increases, there is more thermal energy present within the system to overcome the frictional forces present that contribute to the viscosity. Beyond 318 Kelvin, there is an unexpected upward trend in the viscosities for the 3.5% by mass and 5% by mass solutions of C10E7P2OH. This unexpected trend may be explained by a size increase of the surfactant aggregates with temperature, which increases the friction within the solution. The larger aggregate size at higher temperatures begins to outweigh the increase in thermal energy helping to overcome these frictional forces[6].

**2.3 DOSY Results**

Using diffusion-ordered spectroscopy (DOSY), the diffusion coefficient, *D*, for each component of each solution could be determined across an effective temperature range. This temperature range was previously determined from the cloud point measurements of C10E7P2OH/water solutions of different concentrations. *Figure 16* shows the values of *D* determined for each component of each solution (excluding water) across the effective temperature range.

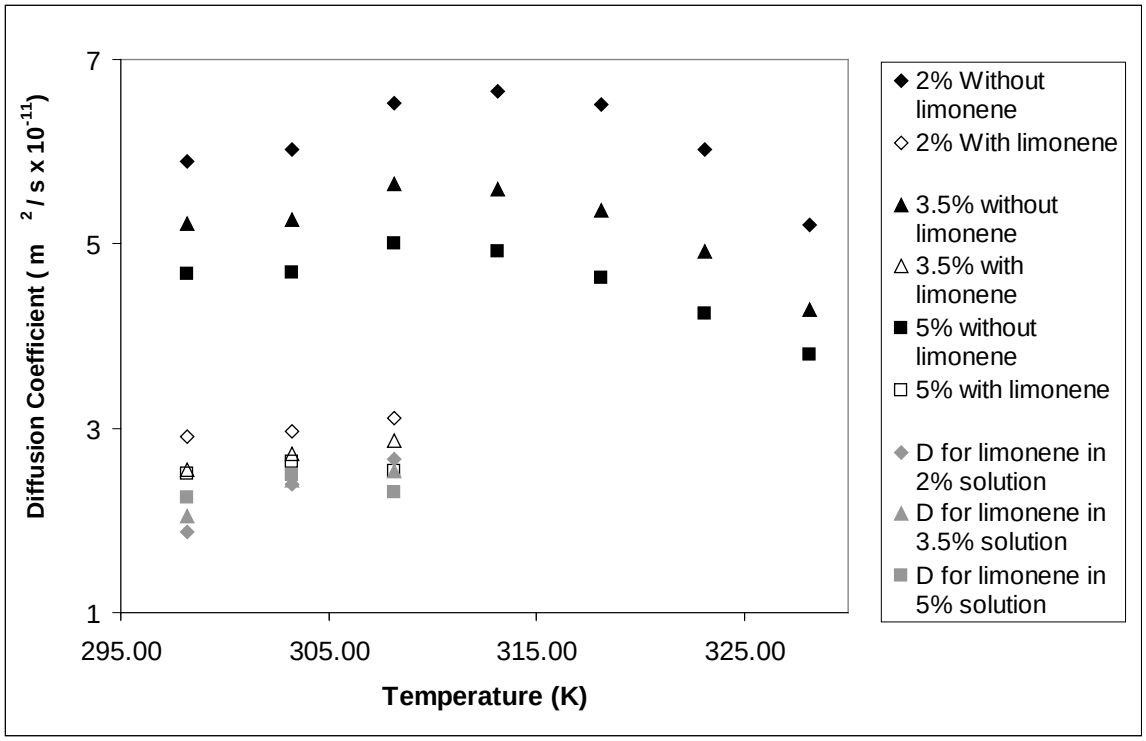


*Figure 16, Diffusion Coefficients determined from DOSY for C10E7P2OH Solutions*

The diffusion data in *Figure 16* and the viscosity data in *Figure 15* provide essentially all of the important data necessary for a complete analysis of the C10E7P2OH surfactant system on a molecular level. The solid black data points in *Figure 16* represent *D* for C10E7P2OH in C10E7P2OH solutions without D-limonene. The white points with thin black outline represent *D* for C10E7P2OH in C10E7P2OH solutions that also contain D-limonene, while the grey data points represent *D* for D-limonene in these same solutions. It is important to note that when comparing solutions of equal concentration of C10E7P2OH with and without D-limonene, the value of *D* is significantly lower for those solutions containing limonene. This indicates that when D-limonene is included in solution, the aggregates swell as the D-limonene is incorporated inside of them, thus causing them to diffuse more slowly.

Also, *D* for the component D-limonene is very similar to *D* for C10E7P2OH within the same solution, although *D* for the D-limonene component is consistently slightly lower. The similarity in these two values indicates that indeed they are diffusing as one entity. If D-limonene were forming its own independent aggregates within the water phase, separate from the surfactant aggregates, then one would expect to see two completely different values of *D* for C10E7P2OH and D-limonene. *D* is however consistently slightly lower for the D-limonene component, which cannot be ignored.

One explanation for the slightly lower *D* values relies on the consideration that D-limonene must slide in and out of the surfactant aggregates regularly. Also, the qualitative observation of the strong lemon odor given off by these solutions indicates that D-limonene is evaporating from solution regularly, and thus not every D-limonene molecule is enclosed permanently by the surfactant aggregates. These D-limonene molecules, when they are in the continuous water phase outside of the surfactant micelles, likely aggregate to microemulsions, which are perhaps even larger than the surfactant micelles, and therefore diffuse at a slower rate then the micelles themselves. Since the *D* value calculated by the pulse program is an average of all of the *D*s for each molecule of that component in solution, an average *D* value for all D-limonene molecules in solution will be lower then *D* for the C10E7P2OH component in the same solution.

### 2.4 Determining Aggregate Size

With viscosity and diffusion coefficients known as a function of concentration and temperature, it is possible to determine the average aggregate radius for each solution

using the Stokes-Einstein Equation, *Equation 2*. A plot of the aggregate sizes calculated from the diffusion and viscosity results is shown in *Figure 17*.

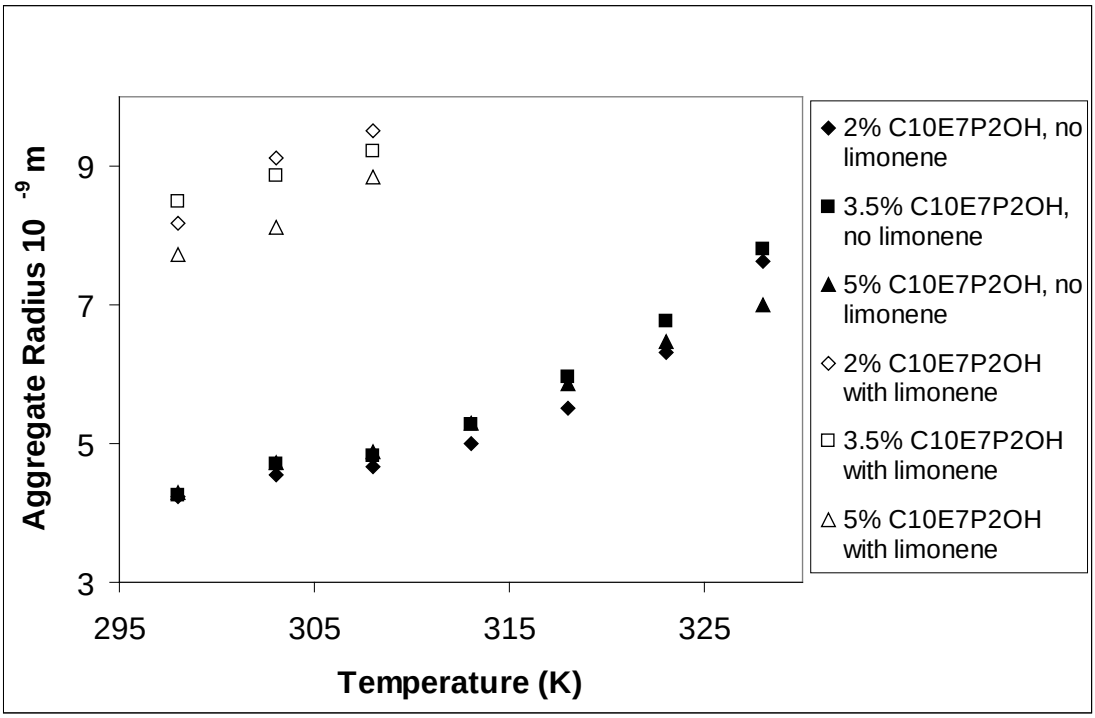


*Figure 17, Aggregate Size for C10E7P2OH solutions*

This upward trend observed across each data set in this plot indicates that as temperature increases, so too does the aggregate size. The solid black data points represent solutions containing no D-limonene, while the solid white data points outlined in black represent solutions with D-limonene. These data clearly show that as D-limonene is incorporated in solution, the aggregate size approximately doubles at each concentration. This provides further evidence that D-limonene is incorporated into the C10E7P2OH micelles, causing them to swell.

Concentration seems to have an uncertain effect on aggregate size, indicating that perhaps the surfactant micelles do not significantly change in size across the various

concentrations, but rather the concentration of aggregates in solution must actually increase.

### 2.5 $T_1$ and $T_2$ Data

The most useful information is obtained from comparing the $T_1$ and $T_2$ time constants. For the surfactant systems studied, a significant difference between $T_1$ and $T_2$ time constants indicates that the environment in which the molecule of interest resides is constrictive, and there are outside interactions occurring which prevent unrestricted relaxation. This evidence would support the hypothesis that surfactant aggregates are forming, and that D-limonene exists within these aggregates.

The $T_1$ and $T_2$ time constants could therefore further support the hypothesis that the C10E7P2OH molecules form large aggregates in solution, and that D-limonene is incorporated within these aggregates. When determining these constants from the spectra obtained from the relevant experiments, each individual signal in the spectra can be integrated across all sixteen slices to give a separate time constant as introduced in section 1.6c. Because the different signals in a spectrum are representative of different nuclei within a molecule, there can be different $T_1$ and $T_2$ time constants for each signal in the spectrum. For the spectra representing C10E7P2OH/D-limonene/water solutions, nine signals were integrated. Five of these signals are from D-limonene and four from C10E7P2OH. *Figure 18* shows an example of a 1D $T_1$ slice of the longest delay time for a C10E7P2OH/D-limonene/water solution, and the labeled nine signals that were integrated across all of the slices. The sample was 3.5% by mass surfactant in $D_2O$ with 2% by mass D-limonene.

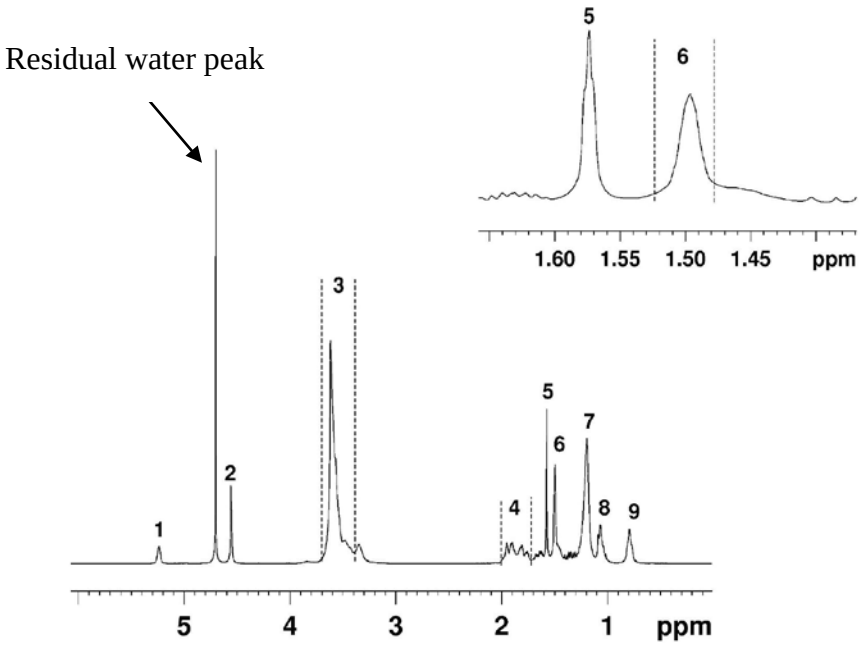


*Figure 18, sample $T_1$ slice showing the signals for which $T_1$ and $T_2$ time constants were determined*

$T_1$ and T2 experiments were conducted on solutions of 2%, 3.5 % and 5% by mass solutions of C10E7P2OH in water containing no D-limonene, as well as solutions of identical C10E7P2OH concentration but containing x% D-limonene. The data for $T_1$ time constants for all 9 signal peaks of solutions containing no-D-limonene are shown in *Figure 19.*

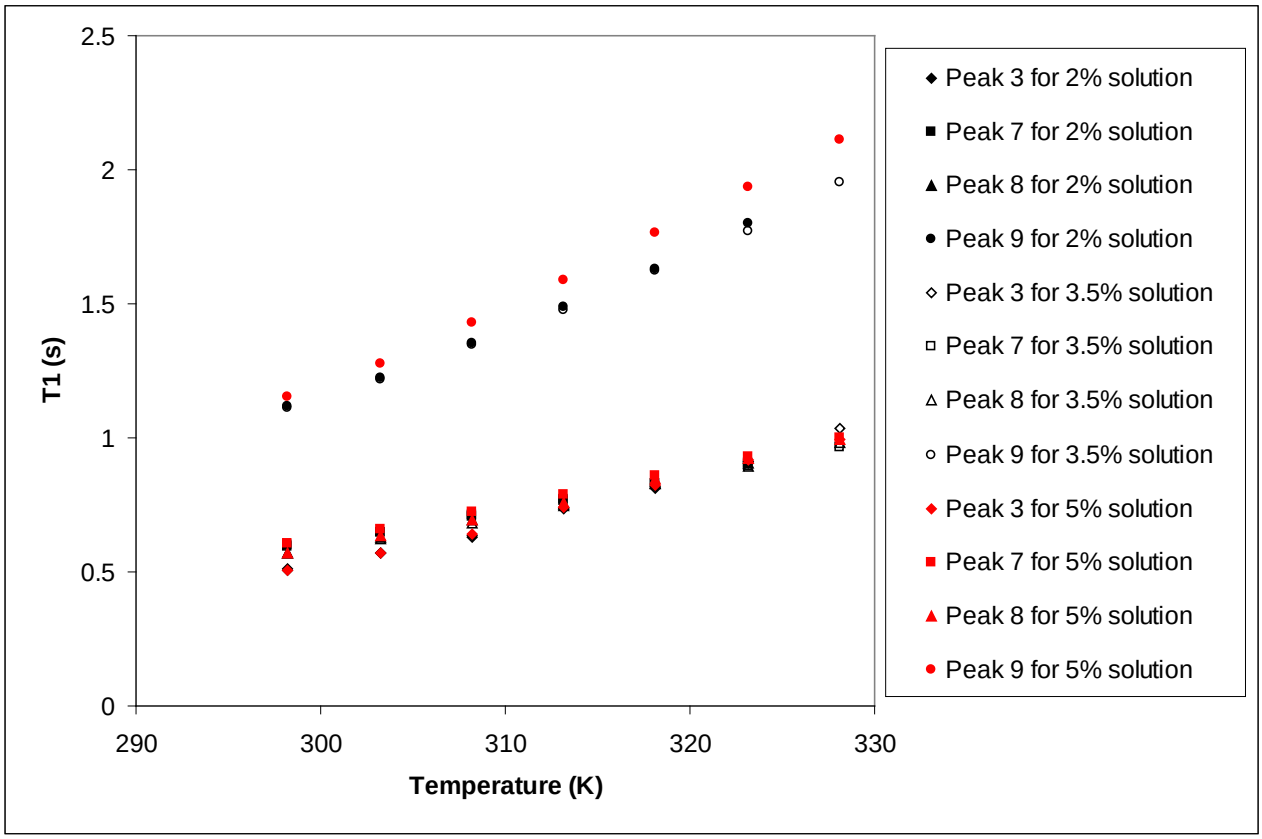


*Figure 19, $T_1$ time constants for solutions containing no D-limonene*

Those data points which are significantly removed from the general trend are from peak 9, which is the peak that represents the end methyl group in the structure for C10E7P2OH. The larger $T_1$ time constant indicates that there is slower relaxation for this nucleus because of the environment in which it resides. The environment that inhibits relaxation must be rigid and allow for less movement. The data is supportive of our hypothesis, since this area of the surfactant molecule should be hypothetically contained well within the aggregate, and therefore inhibited in movement by its crowded environment.

$T_1$ time constant data for solutions containing D-limonene are shown in *Figure 20a, 20b, and 20c.*

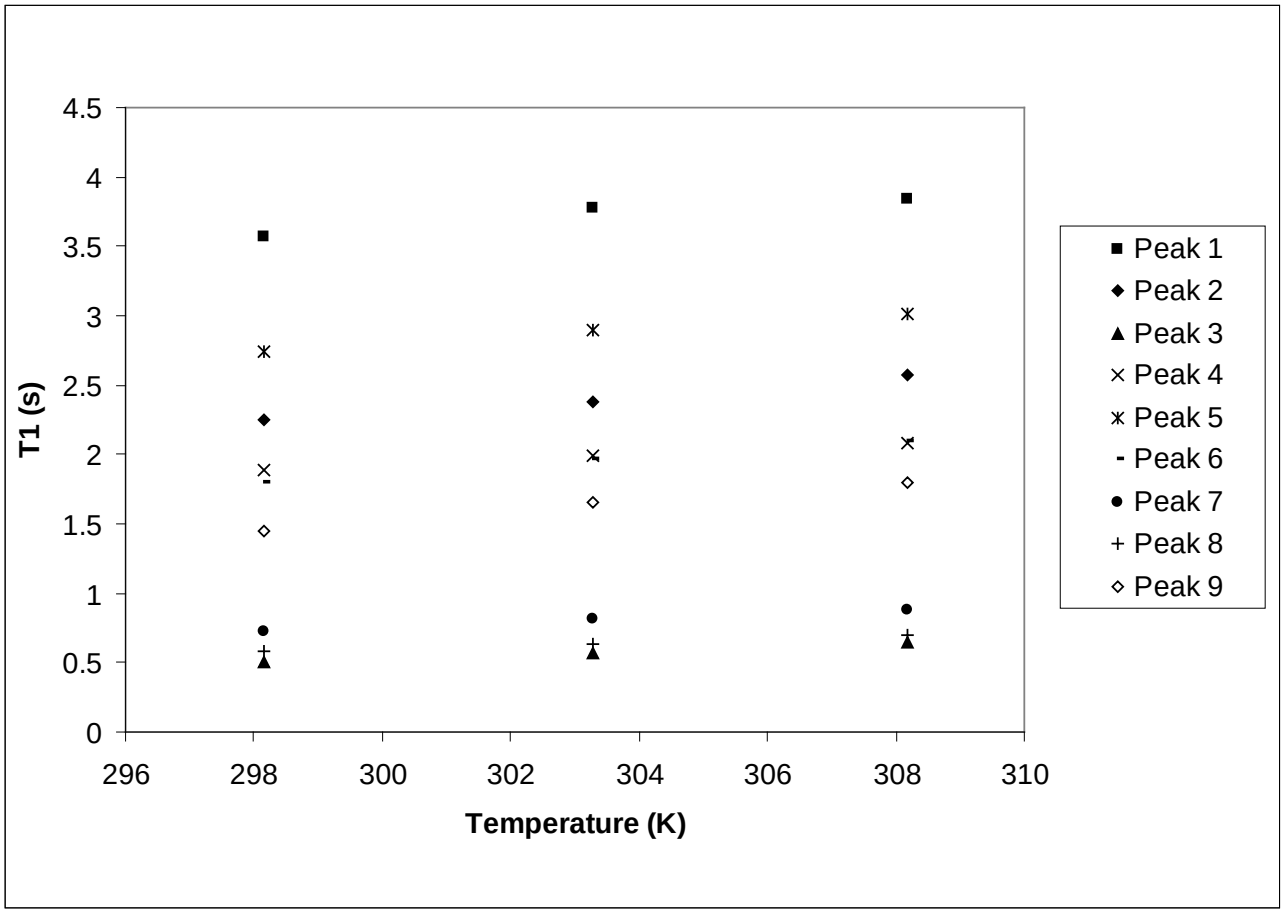


*Figure 20a, $T_1$ time constants for 2% by mass surfactant solutions containing D-limonene*

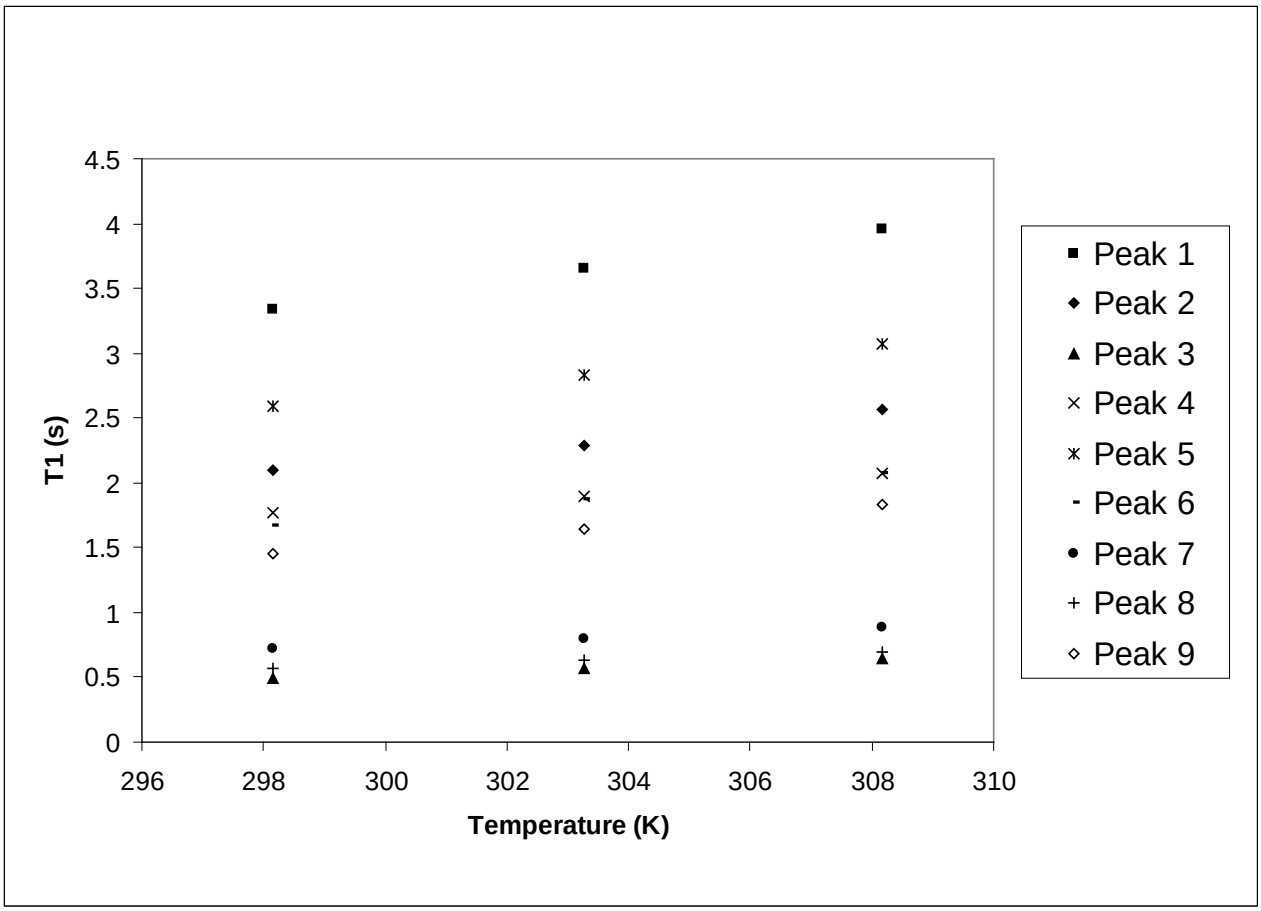


*Figure 20b, $T_1$ time constants for 3.5% by mass surfactant solutions containing D-limonene*

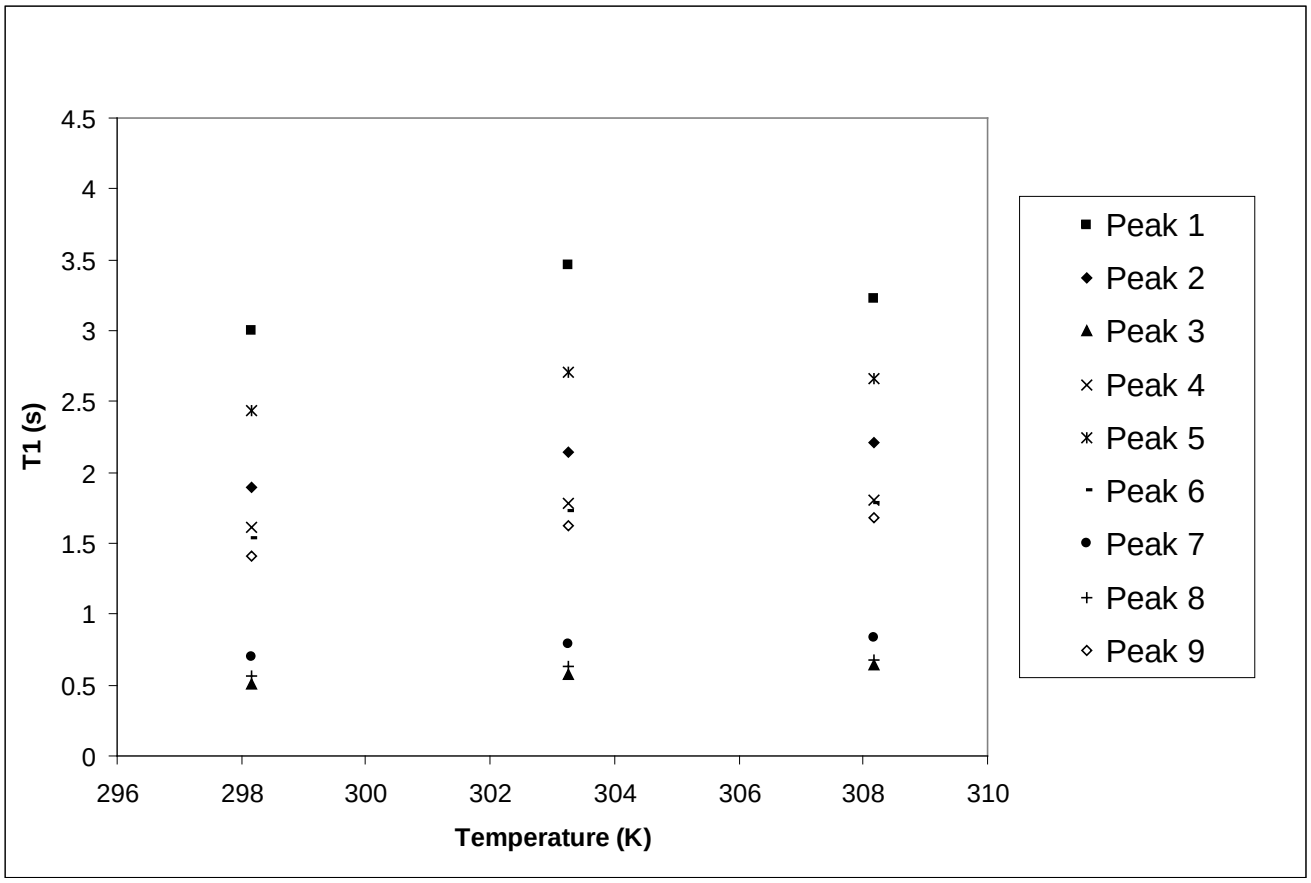


*Figure 20c, $T_1$ time constants for 5% by mass surfactant solutions containing d- limonene*

For these solutions containing D-limonene, the $T_1$ values are all considerably higher then those for solutions that do not contain D-limonene. The range of the y-axis increases from 0-2.5 s to 0-4.5 s to include all of the data after the inclusion of D-limonene in solution. This indicates that the environment of the nuclei represented by each of the nine peaks is more hindered. This corresponds with the prediction that D-limonene associates within the surfactant micelles, making the interior of the micelles more crowded and rigid. The elevation of the $T_1$ time constants for solutions containing D-limonene supports this assumption.

$T_2$ time constants were determined for all nine peaks of the same solutions used previously. The data for these experiments on the solutions containing no D-limonene are shown in *Figure 21*.

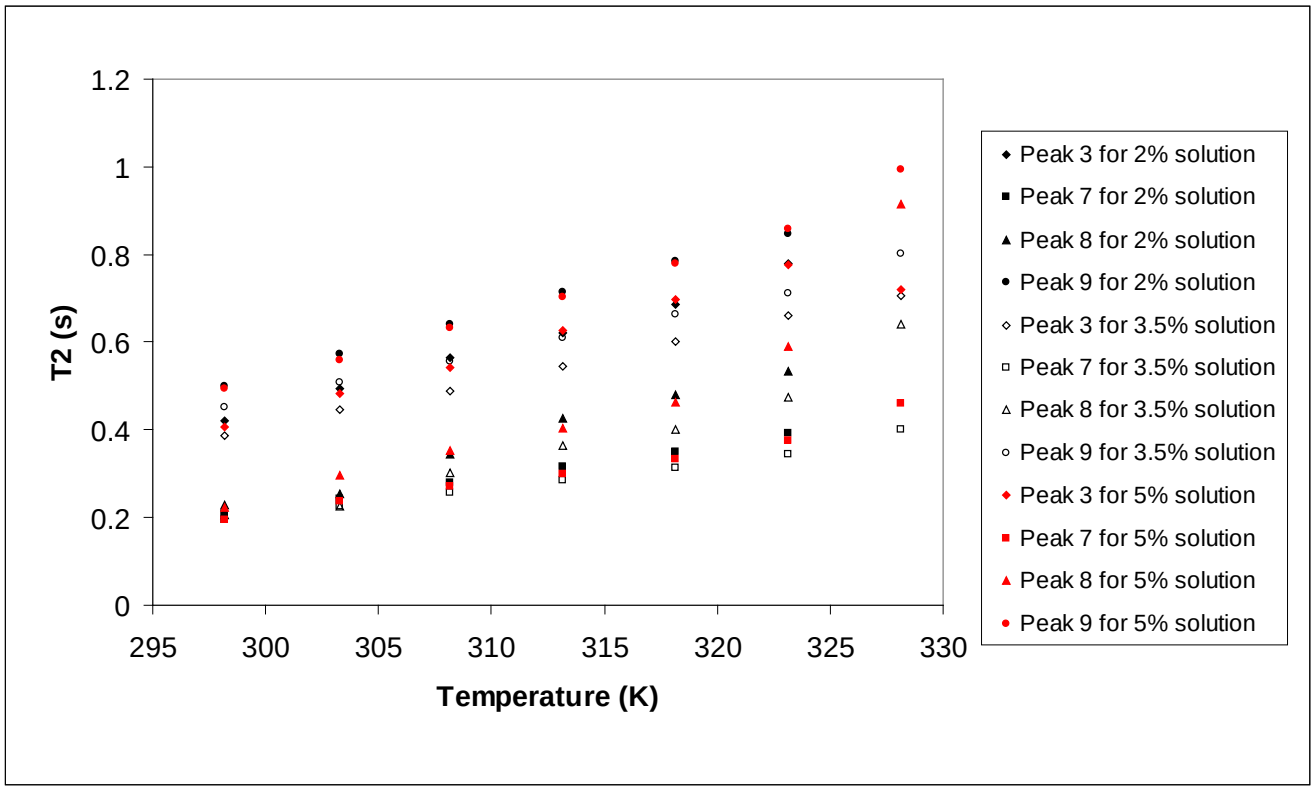


*Figure 21, $T_2$ time constants for solutions containing no D-limonene*

The data for the $T_2$ experiments conducted on the 3 solutions containing D-limonene are shown in *Figure 22a, 22b, and 22c*.

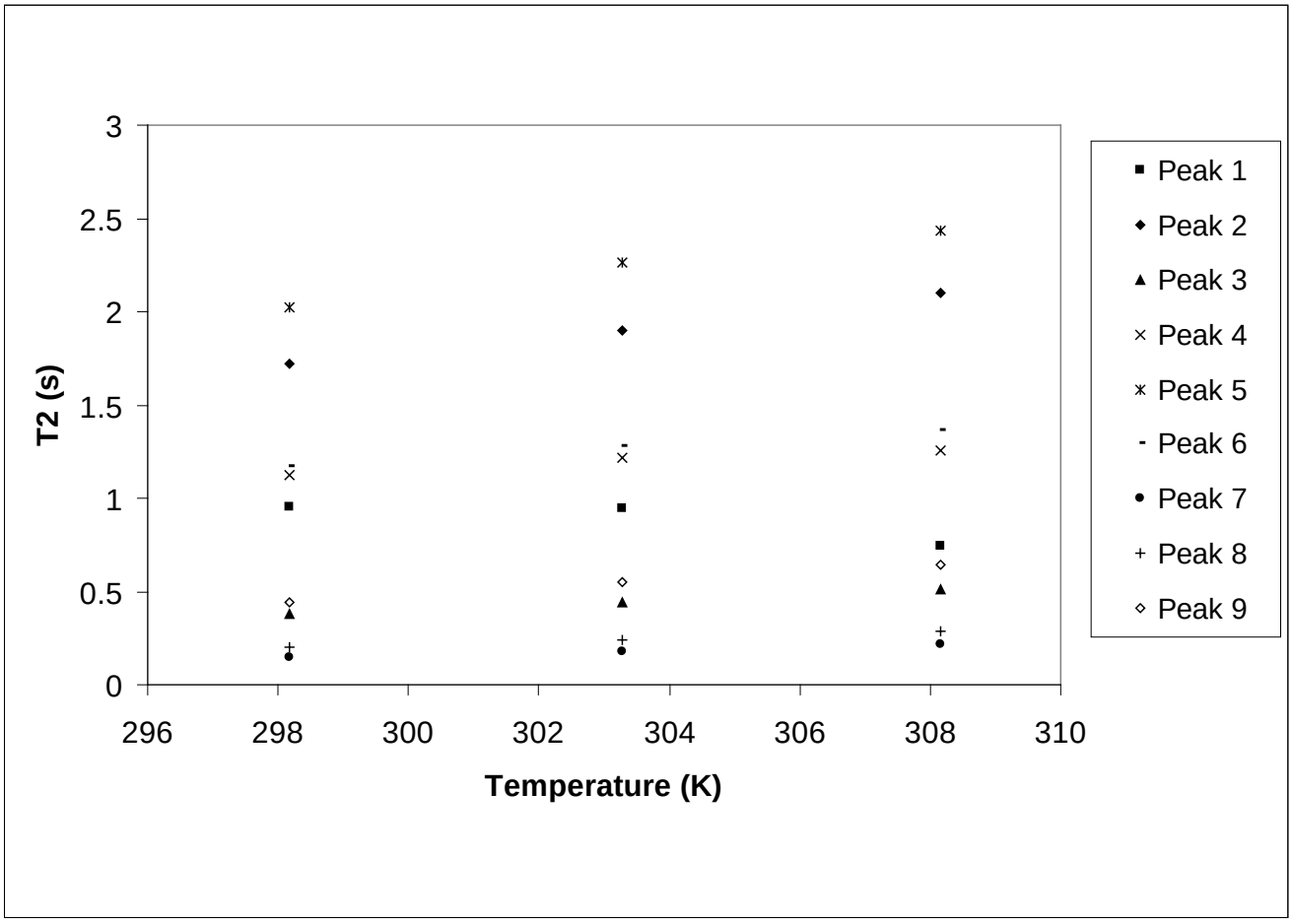


*Figure 22a, $T_2$ time constants for 2% by mass surfactant solutions containing D-limonene*

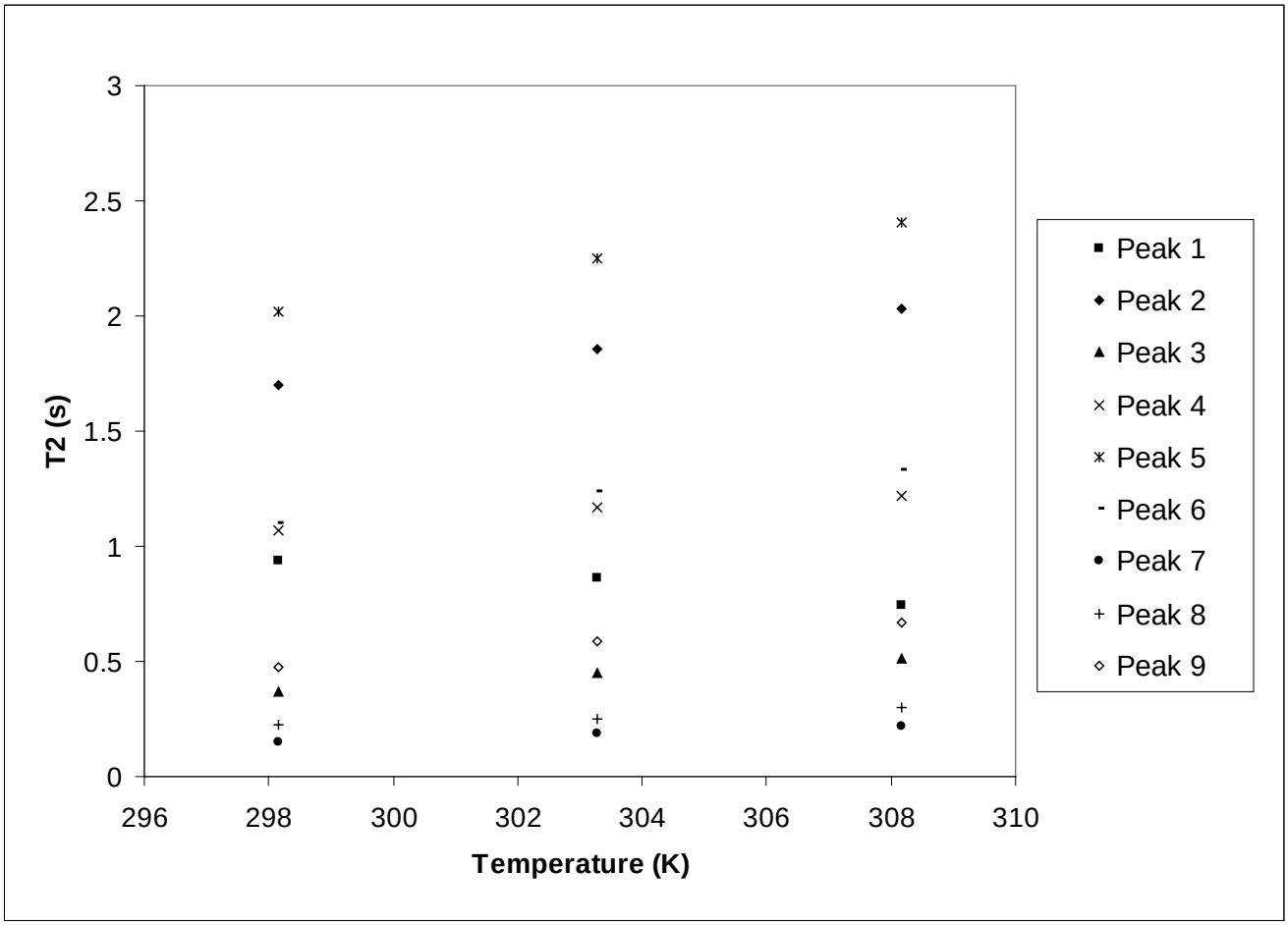


*Figure 22b, $T_2$ time constants for 3.5% by mass surfactant solutions containing D-limonene*

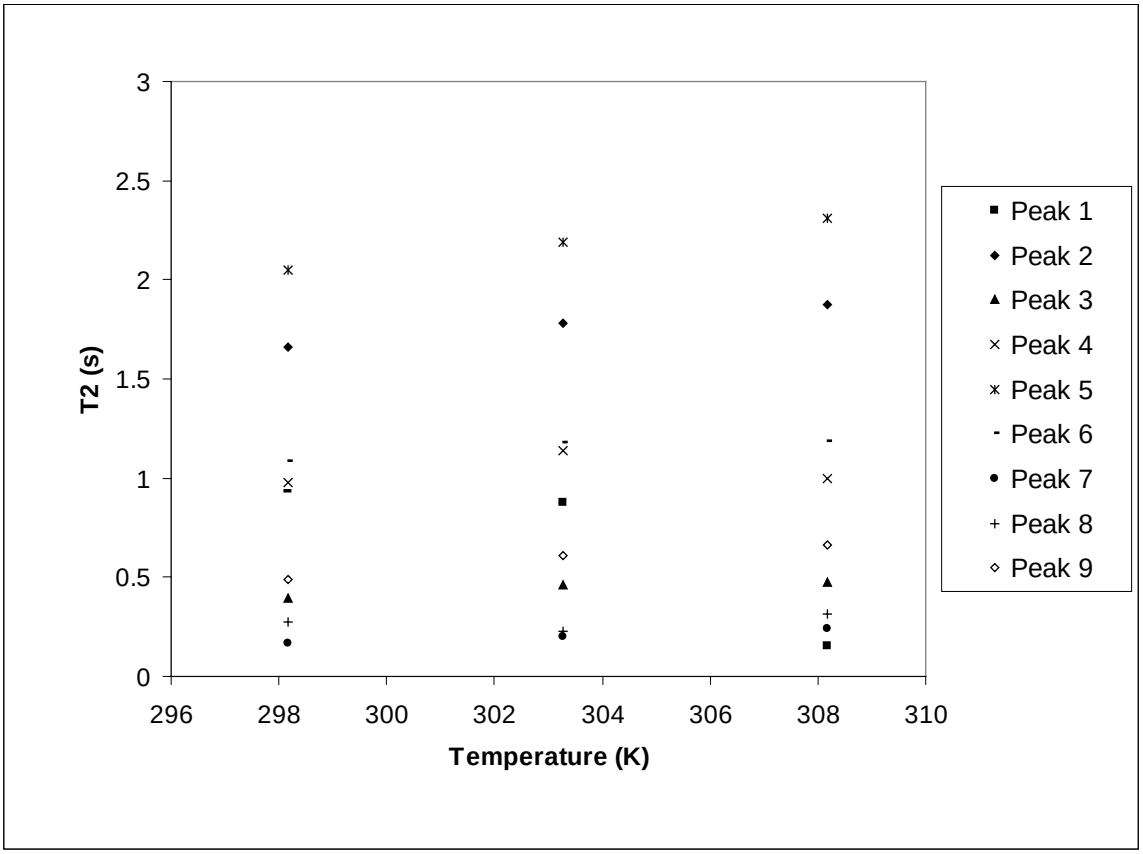


*Figure 22c, $T_2$ time constants for 5% by mass surfactant solutions containing D-limonene*

There is a similar trend for $T_2$ time constant values in these solutions: when D-limonene is added, the values increase. This again supports the existence of aggregates in solution which hinder relaxation of the nuclei. It is also important to note the difference in values for $T_2$ compared to $T_1$. The values for $T_2$ time constant are all within the range 0s to 1.2s, while the values for $T_1$ extend in the range of 0s to 2.5s for these solutions. To clearly illustrate this difference, a comparison of all data points corresponding across temperature and solution type was conducted. One of these comparisons showing the exact $T_1$ and $T_2$ values for the 3.5% by mass solution containing D-limonene is shown in *Table 1*.

*Table 1, $T_1$ and $T_2$ values in seconds for 3.5% by mass C10E7P2OH in water with D-limonene at 308K*

| ***Peak*** | ***1*** | ***2*** | ***3*** | ***4*** | ***5*** | ***6*** | ***7*** | ***8*** | ***9*** |
|---|---|---|---|---|---|---|---|---|---|
| ***$T_1$*** | ***3.961*** | ***2.568*** | ***0.642*** | ***2.072*** | ***3.066*** | ***2.068*** | ***0.879*** | ***0.697*** | ***1.838*** |
| ***$T_2$*** | ***0.743*** | ***2.030*** | ***0.511*** | ***1.218*** | ***2.410*** | ***1.330*** | ***0.217*** | ***0.301*** | ***0.668*** |

$T_1$ and $T_2$ are distinctly different for these solutions. This is evidence that aggregates are forming that restrict the molecular motion in the surfactant and D-limonene molecules because $T_1$ and $T_2$ should be equal in normal liquid solutions where no aggregates are forming. Because the $T_1$ and $T_2$ values differ for peaks that represent nuclei in both surfactant and D-limonene, we can say that both molecules are included in the aggregates in these solutions. This is strong evidence to support the prediction that D-limonene is included within the surfactant micelles.

**2.6 Interpretation of Aggregate Size**

Using all of the data we have collected, especially the values for the aggregate radius, it is possible to determine the aggregate number (average number of surfactant molecules that form an aggregate) for each solution and relate it to the concentration of these molecules in solution. Given that in actuality the surfactant aggregates are in constant flux with respect to chemical exchange and size, the word average here means an ensemble average as well as a time average of the values for the aggregate size and corresponding aggregate number. Thus, in order to determine aggregate numbers using the radius values, it was necessary to establish a few representative models, all representing rigid states for the surfactant micelles. These models were chosen in part to

represent extreme cases to establish upper and lower boundaries for aggregate numbers. This approach is reasonable and ?. A diagram of the principle model of the C10E7P2OH micelles without any D-limonene included, which has been used before in other investigations[2], is shown in *Figure 23*.

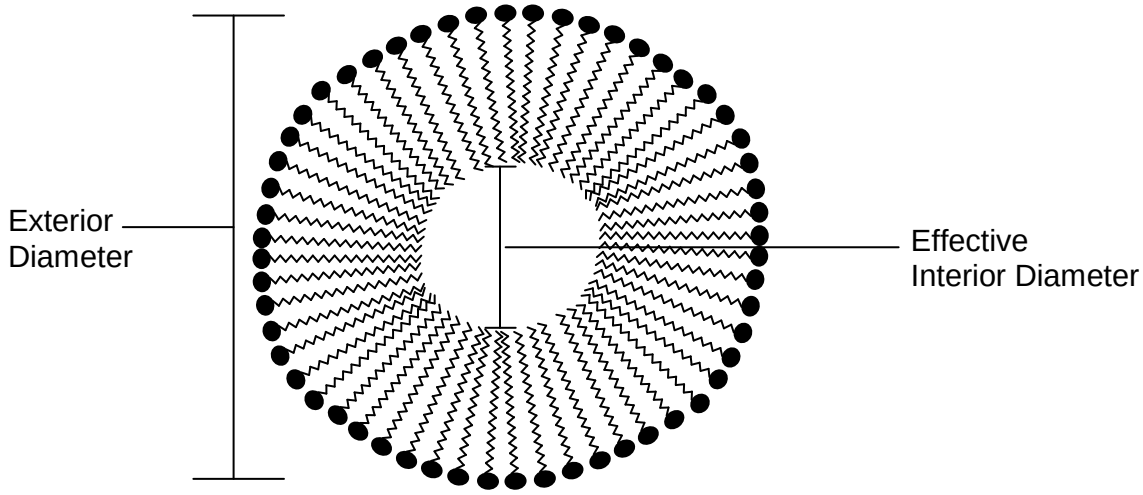


*Figure 23, Model for surfactant micelle without D-limonene*

This image in *Figure 23* is a cross-section of the hypothetical model which assumes the micelle to be a perfect sphere where the surfactant molecules are packed as tightly as possible in a single layer without overlapping their long hydrophobic tails. In order to use values already determined for aggregate radii to determine aggregate numbers, three different arithmetic methods were established by considering extreme cases to determine upper and lower bounds for aggregate number, as well as a more reasonable middle case. For each method, we gave surface area and volume different weights in determining how the surfactant molecules can pack as tightly as possible into a single layer, spherical micelle like the one shown in *Figure 23*.

In order to calculate the aggregate number from Method 1 we used the following ratio:

$$\frac{\text{Micelle inner pocket surface area}}{\text{Surfactant molecule surface area at end methyl group}}$$

This method assumes that the surfactant molecules are packed as tightly as they possibly can be at their ends in the interior of the micelle, and that the surfactant molecules do not overlap. This model represents an extreme case where the surfactant molecules are the least dense they could possibly be in the aggregates, therefore providing an underestimate of the actual aggregate number.

Method 2 can be used to determine aggregate number by the following ratio:

$$\frac{\text{Micelle outer surface area}}{\text{Surfactant molecule surface area at terminal hydroxyl group}}$$

This method assumes the surfactant molecules to be packed as tightly as possible along the outside surface of the micelle. In order for this to be possible, the long hydrophobic tails must overlap considerably more than they possibly could in the smaller interior of the micelle. This is an extreme case where an exorbitant number of C10E7P2OH molecules must overlap and squeeze into a small micelle interior, therefore providing an overestimate of the actual aggregate number

Method 3 can be used to determine the aggregate number by the following ratio:

$$\frac{\text{(Total micelle volume – inner pocket volume)}}{\text{Volume of one C10E7P2OH surfactant molecule}}$$

This method assumes that the surfactant molecules are packed tightly into a single layer without overlap. Also, this model accounts for the “empty” inner pocket by subtracting

its volume from the total volume of the micelle. It is important to note that there cannot actually be a true empty pocket in the micelle at any given time. This pocket can instead be considered a less dense region, as the micelle is fluid, with surfactant molecules shifting towards and away from the interior of the micelle. The single layer model with the empty pocket provides a static model of an average state for a micelle. This model provides a reasonable estimate of aggregate number because it accounts for the volume of the micelle that should be occupied by a single layer of tightly packed C10E7P2OH molecules, which is indeed the general model represented in *Figure 23*.

Each method was applied to the aggregate radii data and values for aggregate number were determined for each solution across the temperature range previously analyzed. A comparison of the values for a 3.5% by mass solution of C10E7P2OH in water without D-limonene is shown in *Table 2*.

*Table 2, Aggregate Numbers in 3.5% C10E7P2OH in water without D-limonene*

| Solution | Temperature (K) | Aggregate # Low Estimate (Method 1) | Aggregate # High Estimate (Method 2) | Aggregate # Middle Estimate (Method 3) |
|---|---|---|---|---|
| 3.5% C10E7P2OH in D2O without D-limonene | 298 | 9 | 806 | 301 |
| | 303 | 37 | 987 | 405 |
| | 308 | 47 | 1035 | 434 |
| | 313 | 97 | 1237 | 560 |
| | 318 | 207 | 1577 | 785 |
| | 323 | 392 | 2037 | 1108 |
| | 328 | 714 | 2710 | 1605 |

This data in *Table 2* show that Method 3 is indeed the most reasonable method, yielding values which fall almost directly in between the two boundary values determined using Method 1 and Method 2. Also, a study on similar non-ionic surfactant micelles

forming in solution with water indicates that the aggregation number for these surfactant types is between 50 and 100 at 298K[15]. This indicates that method 1, which estimates an aggregate number ~10 is an underestimate, while method 2, which estimates ~1000, provides an overestimate of the true aggregate number. A value that better corresponds with previous literature is obtained from method 3 (~300)[15]. Once Method 3 was determined to be a reasonable estimate of aggregate number, the values across all solutions at every temperature analyzed were determined. These data are shown in *Figure 24.*

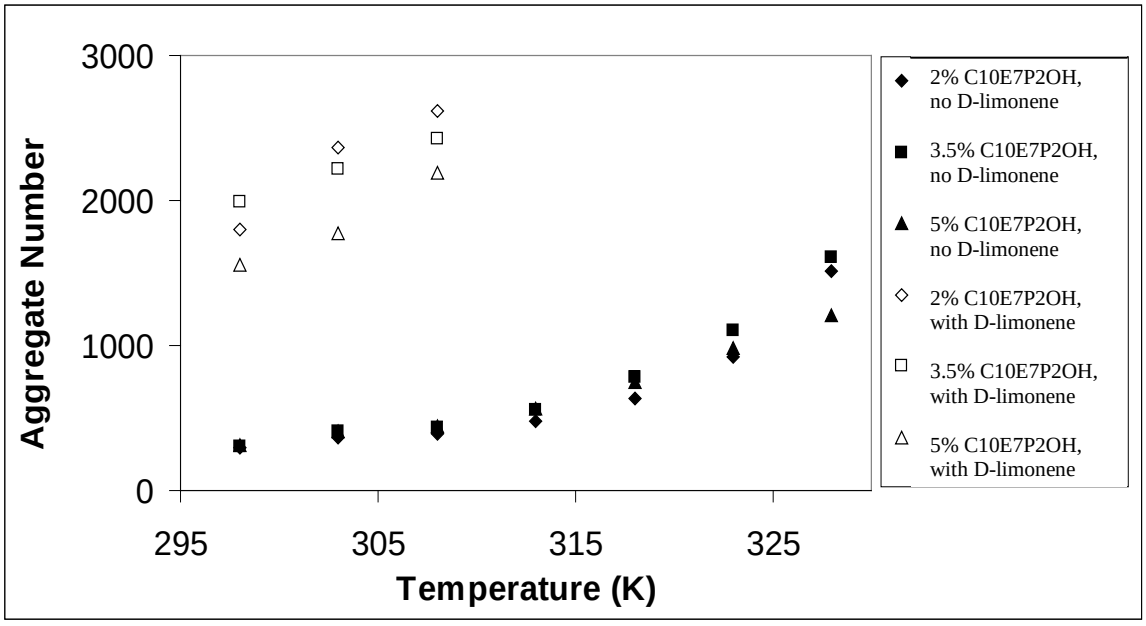


*Figure 24, Surfactant aggregate number for all solutions*

The solid data points represent aggregates in solutions not containing D-limonene, while the white data points with black outline represent aggregates in solutions with D-limonene. These data clearly support the previous observation that aggregate size increases as D-limonene are added. There is no significant observable trend in aggregate size across solutions of varying concentration for solutions not containing D-limonene.

| C10E7P2OH |
|---|

For solutions containing D-limonene however, as surfactant concentration decreases, aggregate size increases. This indicates that as more surfactant is present in solution, the D-limonene molecules can be distributed over more micelles, therefore decreasing the average micelle size. As D-limonene is included in solution, the aggregate number increases significantly. This means that if D-limonene is not included in the actual walls of the micelle, more molecules must gather to form a bigger micelle that includes D-limonene within its interior.

### 2.7 Determining Where D-limonene Associates

Additional models were established to predict how D-limonene was associating within the surfactant micelles, and how many D-limonene molecules on average could be part of the micelle. The two models that were considered to be valid are shown in *Figure 25.*

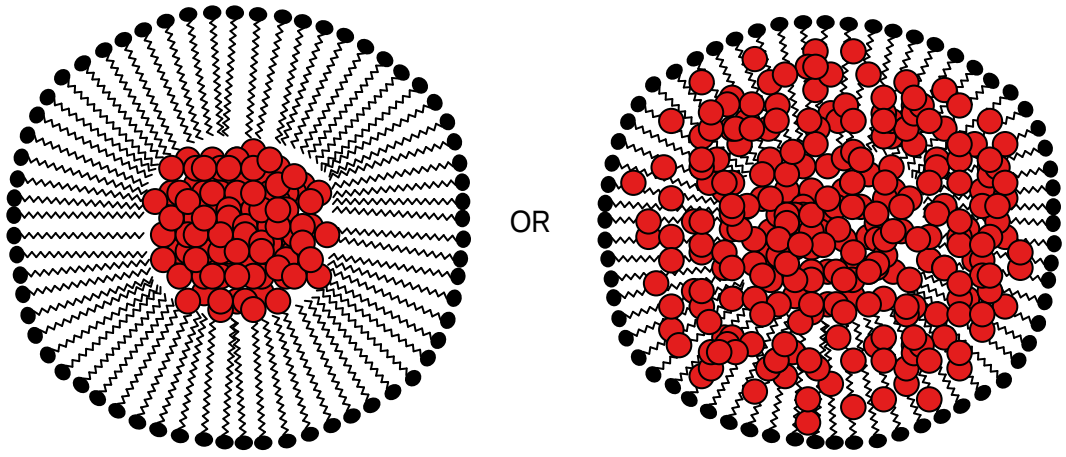


*Figure 25, Two models predicting the association of D-limonene within micelles*

Model A assumes that D-limonene molecules are not included in the walls of the surfactant micelle, but instead are contained entirely within a tightly packed interior formed by the surrounding surfactant molecules. Model B considers that the D-limonene molecules, being hydrophobic, may be included within the walls of the micelle, among the long hydrophobic tails of the surfactant molecules. In a manner similar to the analysis done to determine aggregate number, two arithmetic methods were establish to estimate the number of D-limonene molecules included in the micelles.

Method A was established to represent the scenario where all of the D-limonene molecules are contained in an inner pocket and not associated within the walls of the micelle. It is represented by the following ratio:

$$\frac{\text{Volume of inner pocket}}{\text{Volume of one D-limonene molecule}}$$

This model assumes no overlap of D-limonene molecules, and no overlap of D-limonene with the surfactant molecules that form the aggregate, and therefore should provide a low boundary for an estimate of the number of D-limonene molecules included within the micelles.

Method B was established to represent the scenario where D-limonene can also be part of the aggregate wall. It is represented by the following ratio:

$$\frac{\text{Change in volume of aggregate after D-limonene is added (constant solution concentration and temperature)}}{\text{Volume of one D-limonene molecule}}$$

This model accounts for the possibility of the D-limonene molecules associating anywhere within the interior of the micelle, including amongst the surfactant molecules in the micelle wall. It considers the swelling of the surfactant aggregates once D-limonene is added to solution to be due entirely to the inclusion of D-limonene within the aggregates. It also assumes that the volume of the aggregate increases by the volume of the D-limonene molecules included exactly, and therefore the aggregate is no more or less compact after the inclusion of the D-limonene molecules than it was before. Since it is more probable that the D-limonene being included actually causes the micelle to become more compacted, this estimate provides an upper boundary for the number of D-limonene molecules enclosed.

For the 3.5% by mass solution of C10E7P2OH in water with D-limonene, the values for number of D-limonene enclosed within the aggregates are shown in *Table 3.*

*Table 3, Estimate of the number of D-limonene enclosed within a surfactant aggregate*

| Solution | Temperature (K) | Aggregate # Low Estimate (Model A) | Aggregate # High Estimate (Model B) |
|---|---|---|---|
| 3.5% by mass C10E7P2OH in water with D-limonene | 298 | 24 | 84 |
| | 303 | 30 | 59 |
| | 308 | 37 | 164 |

It is important to note that the number of D-limonene molecules included within the micelles is relatively low compared to the number of surfactant molecules contained in the sample. If, for example, standard 2g samples of each solution were made and used for NMR analysis and if the solution was 3.5% by mass C10E7P2OH in water with D-limonene, then

- The number of surfactant molecules = $1.18 \times 10^{-4}$ mol

- The number of D-limonene molecules = 2.94 x $10^{-4}$ mol
- The ratio of D-limonene molecules / surfactant molecules = 2.49/1

The same ratio of D-limonene molecules to surfactant molecules for the aggregates within this solution can be determined across various temperatures, and even using the upper boundary estimate, it is certain that there are too many D-limonene molecules in solution to be entirely contained within aggregates. These data are shown in *Table 4.*

*Table 4, Estimated composition of aggregates in 3.5% by mass solution of C10E7P2OH in water with D-limonene, using upper boundary estimate for D-limonene included*

| *Temperature (K)* | *# Surfactant Molecules/ Aggregate(best estimate)* | *# D-limonene Molecules/ Aggregate (high estimate)* | *Limonene / Surfactant Molecules* |
|---|---|---|---|
| *298* | *301* | *84* | *0.28 / 1* |
| *303* | *405* | *59* | *0.15 / 1* |
| *308* | *434* | *164* | *0.38 / 1* |

The data show that across the three temperatures for this one solution, between 85% and 94% of the D-limonene molecules in solution are not included within the surfactant aggregates using the upper boundary estimate. This trend is consistent across all of the solution concentrations analyzed, therefore the D-limonene must be elsewhere in solution, or the composition of the aggregates must be more complex then the models exhibit. The data obtained from the DOSY experiments and also $T_1$ and $T_2$ experiments support the hypothesis that the D-limonene is incorporated into the micelles, so there must be an explanation for the remaining D-limonene molecules in solution.

It was observed during the study that D-limonene is substantially volatile because of the strong lemon odor it exudes. This would indicate that there are D-limonene molecules readily evaporating from solution and therefore temporarily contained in the

water phase, outside of the surfactant aggregates. Since D-limonene incorporates itself into the surfactant micelles when added to solution, but also must be present in the water phase before it evaporates, then it must be able to pass readily through the walls of the surfactant micelles. If, however, the majority of the D-limonene molecules resided within the water phase of these solutions and does not exchange rapidly with the D-limonene molecules within the micelles, then the DOSY results should show two distinctly different diffusion coefficients for D-limonene and surfactant, as the D-limonene molecules may form separate aggregates. The data showed very similar diffusion coefficients though, indicating a fast D-limonene exchange with the micelles.

### 2.8 Number of Micelles in Solution

To provide a general idea of the concentration of micelles in a standard solution like the ones analyzed in this study, a standard 2g, 3.5% by mass C10E7P2OH in water solution containing D-limonene was considered. *Table 5* shows the calculated concentrations for this sample across the three temperatures analyzed.

*Table 5, Concentration of surfactant micelles in 3.5% by mass C10E7P2OH in water solution containing D-limonene*

| Temperature (K) | # Surfactant Molecules/Aggregate (best estimate) | # of Aggregates | **Concentration of Aggregates in solution (mM)** |
|---|---|---|---|
| 298 | 301 | $2.36 \times 10^{17}$ | **0.196** |
| 303 | 405 | $1.75 \times 10^{17}$ | **0.145** |
| 308 | 434 | $1.64 \times 10^{17}$ | **0.136** |

The data show that the typical micelle concentration of these solutions is in the tenth millimolar range. In the same 3.5% by mass surfactant solution, since D-limonene was added at 2% by mass as well, the concentration of D-limonene molecules is 147 mM.

This means that D-limonene molecules exceed surfactant micelles by a factor of about 1000. A single micelle cannot incorporate nearly this many D-limonene molecules, as the NMR data has shown in this study.

## 3. Experimental

### 3.1 Preparation of NMR Samples

The origin of the surfactant C10E7P2OH that was used to prepare all of the samples is shown in *Table 9*.

*Table 9, Surfactant Information*

| Label | Chemical name (vendor name) | CAS # | Vendor |
|---|---|---|---|
| 29 | Poly(ethylene oxide, propylene oxide) alcohol, branched (Antarox LA-EP-16) | 37251-67-5 | Rhodia |

Pure D-limonene and $D_2O$ were used in combination with this surfactant to prepare samples. Any $H_2O$ contamination of the samples would cause the presence of an extraneous water peak in the NMR spectra which could interfere with the data. For this reason, great care was taken to ensure minimal water contamination in the samples. Also any paramagnetic oxygen gas impurities in the samples would potentially damage the accuracy and precision of the $T_1$ and $T_2$ data, so precautions were taken to avoid this as well.

The procedure for preparing these samples began by vacuum pumping the surfactant sample overnight, as to remove any water impurity already in the sample. The sample was immediately sealed after being removed from the vacuum, and transported into a nitrogen glove box, where it is separated from atmospheric moisture. Mixing of the samples was performed inside of the glove box in 10mL Erlenmeyer flasks, and a portion was withdrawn (~1 mL) and inserted into a glass NMR tube and capped. Once inserted into NMR tubes, samples were removed individually from the glove box for freeze-pump-thawing to remove any gas impurities. All contact with the atmosphere outside of

the glove box was limited to brief (less then one second) exposures, for example when the cap was removed to attach the sample to the vacuum pump for freeze-pump-thawing.

The procedure for freeze pump thawing begins by first attaching the NMR tube to a vacuum pump using vacuum tubing. The sample is frozen using a Styrofoam cup filled with liquid nitrogen by introducing the cup around the NMR tube slowly ensuring that the tube does not crack. Once the sample is completely frozen, the vacuum is turned on, and a vacuum is established inside the tube. The tube is then backfilled with nitrogen gas to around -10 PSI relative to atmospheric pressure. The sample is allowed to thaw by surrounding it with a cup of room temperature water (ensuring it does not crack the tube because of sudden thermal shock). Once thawed, the procedure is repeated for a total of 7 freeze-pump-thaw sequences. After the seven cycles, the still frozen sample is flame sealed with a blow torch about an inch from its insertion into the vacuum tubing, so that it never is exposed to the atmosphere.

The compositions of the entire sample portions for each of the 6 samples are shown in *Table 10*. Note that only a portion of these samples (~1mL) were inserted into each NMR tube.

*Table 10, Composition of 6 final sealed samples*

| CHEM 29 (g) | $D_2O$ (g) | D-limonene (g) | Total mass (g) | % by mass CHEM 29 in solution (%) |
|---|---|---|---|---|
| 0.038 | 1.897 | 0 | 1.935 | 1.964 (2.0) |
| 0.073 | 1.987 | 0 | 2.060 | 3.545 (3.5) |
| 0.109 | 2.097 | 0 | 2.206 | 4.95 (5.0) |
| .045 | 2.233 | 0.040 | 2.318 | 1.98 (2.0) |
| .069 | 1.891 | 0.040 | 2.000 | 3.52 (3.5) |
| .098 | 1.894 | 0.041 | 2.029 | 4.92 (5.0) |

The mass percentage of D-limonene in each of the solutions in containing d-limonine was around 2% by mass.

### 3.2 NMR Experiments

All of the DOSY, $T_1$ and $T_2$ experiments were conducted on a Bruker Avance 300 NMR Spectrometer. It is important to note that the pulse program that was used to obtain diffusion coefficients had designed into it compensation for eddy currents and convection currents that would otherwise adversely affect accuracy. Various parameters for the pulse programs were explored and optimized. These parameters include the relaxation delay time (D1) in seconds, the field strength range across which the scans are made (Initial and Final Field Strength) which was determined to be optimally 10%-100%, the number of scans (NS), the number of dummy scans (DS), the diffusion time (D20) in seconds, and the gradient pulse duration (P30) in microseconds, the size of the FID (# of slices), the pre-scan delay (DE) in microseconds as well as parameters D21 and P19 (in seconds and microseconds respectively). The final optimized parameters are listed in *Table 6*.

*Table 6, Optimized parameters for the experiments T1, T2, and DOSY*

| | **T1** | **T2** | **DOSY** |
|---|---|---|---|
| Size of FID (# slices) | 12 | 12 | 16 |
| DS (dummy scans) | 0 | 0 | 0 |
| NS (# scans) | 8 | 8 | 16 |
| DE (pre scan delay, µs) | 6 | 6 | 6 |
| D1 (relaxation delay, s) | 20 | 15 | 15 |
| D20 (echo time, s) | N/A | 0.001 | 0.5 |
| D21 (s) | N/A | N/A | 0.005 |
| P19 (µs) | N/A | N/A | 200 |
| P30 (µs) | N/A | N/A | 6000 |

Also important for T1 and T2 experiments are the parameter lists: VDlist (T1 delay times in seconds) and VClist (T2 delay in spin echo sequences). These lists represent the delays allowed for each successive slice and are shown in *Table 7* and *Table 8.*

*Table 7, VDlist for T1 Experiment*

| Delay Time (s) |
|---|
| 0.01 |
| 0.02 |
| 0.05 |
| 0.1 |
| 0.3 |
| 0.5 |
| 0.7 |
| 1 |
| 3 |
| 6 |
| 9 |
| 25 |

*Table 8, VClist for T2 experiment*

| Delay Time (# spin echo sequences) |
|---|
| 2 |
| 8 |
| 20 |
| 50 |
| 100 |
| 200 |
| 400 |
| 800 |
| 1000 |
| 1500 |
| 2500 |
| 5000 |

Once optimal parameters had been established, automated data acquisition was done overnight. When the results from automated acquisition were compared against those from experiments run manually there was no discrepancy, indicating that precision and accuracy was not lost in automation. An annotated version of the syntax for one of

the automation setup programs (for the DOSY experiments) is shown in *Appendix A*. It is important to note that the samples were not rotated during the experiments, because rotation would disturb the sample and possibly impact diffusion coefficient or relaxation results. The automation setup programs for the $T_1$ and $T_2$ experiments were the same, except the code line “XAU("dosy 10 100 32 l y")” which initiated the DOSY pulse program was replaced with an initiation of the $T_1$ and $T_2$ pulse programs.

The automation was performed overnight on all six surfactant samples. In total, 18 experiments were performed every night for one particular temperature. Changing temperature during automation introduced complications for the automated programs and erratic results. For this reason, experiments were only run at one temperature each night.

### 3.3 Temperature Calibration

It was necessary to evaluate the accuracy of the temperature setting within the Bruker software TOPSPIN 1.3 which was used to conduct all of the experiments on the NMR instrument. This is because the “set temperature” parameter in the program is not the actual temperature at which the sample is kept during the scans of an experiment. A calibration curve already existed for the instrument, but it was one year old, and a new calibration curve was established to ensure measurement accuracy.

This curve was developed by using a pre-existing program in TOPSPIN called “calctemp”, which calculates the actual temperature of the sample at the time of the scan by determining the chemical shift difference in the two peaks of a proton spectrum of either glycol or methanol. We chose to use a sealed sample of pure glycol for this process.

The temperature calibration curve obtained using the program calctemp is shown in *Figure 26.*

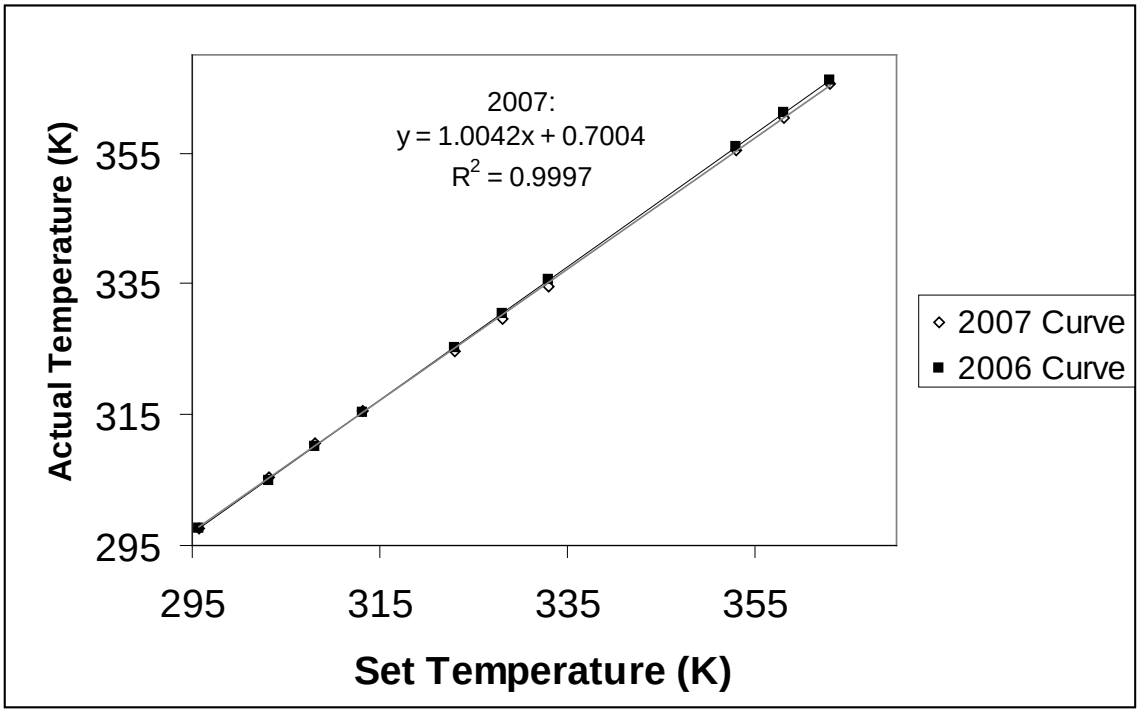


*Figure 26, Calibration curve for edte Set Temperature and Actual Temperature in NMR instrument*

*Figure 26* shows a slight difference between the calibration curves for 2007 and 2006 indicating that this is indeed a necessary step in order to ensure optimal accuracy for the NMR experiments.

### 3.4 Determining Field Gradient Strength

Preliminary DOSY experiments indicated that the field gradient strength of the instrument (which is specified by the user in the Bruker software) was not correct. All of the diffusion coefficient values were greater than the reported values in the literature. In

order to ensure that the D values obtained for the trials on the surfactant systems were accurate, the actual true field gradient strength was calculated by running multiple trials on pure water, chloroform, and cyclohexane samples, all with known D values reported in the literature[5]. Thirteen experiments were run on pure water samples maintaining consistent parameter settings, as well as three experiments on chloroform, and two on cyclohexane. The determined values for D were compared to the literature values for the corresponding identity, and a ratio was determined ($D_{determined}/D_{literature}$). This ratio, combined with *Equation 1* was used to determine the error in the previously inputted field gradient strength, *g*.

$$I = I_o e^{-D\gamma^2 g^2 \delta^2 (\Delta - \delta/3)} \qquad (1)$$

It was determined that the actual field gradient strength, *g*, was 55.6 G/cm compared to a previously reported value of 53.5 G/cm. This new value was declared in the Bruker TOPSPIN 13 software in order to ensure optimal accuracy for D values obtained.

### 3.5 Phase Behavior Investigation

In order to determine the viable temperature range for the NMR experiments, an investigation into the surfactant solutions was performed to determine at what temperature there was a phase transition from a one-phase to two-phase solution. This investigation was performed by slowly heating a 500mL beaker of water on a stirring-hot plate. Suspended in this beaker was a test tube filled with a surfactant solution (pure surfactant in water) of a given concentration, and inside which a mercury thermometer was placed. A stir vane was placed inside of the test tube, and the beaker and the stir function of the hot plate was turned on. The cloud point was determined by visual

observation, and was the first observed point at which the solution became cloudy-white as opposed to its initial clear appearance. The concentration of the solution was plotted against its corresponding cloud point temperature to obtain the phase diagram shown in *Figure 14.*

For solutions containing surfactant, D-limonene, and water, the phase behavior was slightly more complex. Cloud points were observed around 30-35 centigrade as opposed to 50-55 centigrade for just surfactant/water solutions. This investigation provided the basis for our valid temperature range because solutions containing separate phases yielded bizarre data upon conducting DOSY, $T_1$ and $T_2$ experiments. All experiments were therefore conducted within the temperature range which allowed for a single-phase solution. This range was 298.16-308.17 Kelvin for solutions containing D-limonene, and 298.16-328.14 K for solutions that did not contain D-limonene.

### 3.6 Viscosity Investigation

In order to calculate aggregate radii from the Stokes-Einstein Equation, viscosities needed to be determined for every solution composition at every temperature analyzed. This was accomplished by passing each of the six solutions (3 containing D-limonene, 3 without) through viscosimeters kept constant at each temperature of interest in a water bath with automatic temperature control. Viscosimeters of gauge 100 and gauge 200 were used, and the viscosity values determined from the different trials were averaged. *Equation 4* allows determination of the viscosity of each solution using the density of the solution ($\rho$), the apparatus constant ($B$), and the time to pass through the column of the viscosimeter ($t$).

$$\eta(t) = \rho Bt \qquad (4)$$

The density of each solution was known and the time to pass through the viscosimeters column was determined experimentally. The apparatus constants were previously determined by conducting trials at each temperature of interest on pure water of known density and viscosity. The apparatus constants as determined from all of the trials were averaged to obtain the apparatus constants to be used for calculating the viscosity of each surfactant solution.

The density of each solution was determined at room temperature (25 ºC) and extrapolated to provide a density for every temperature up to 60 ºC in increments of 5ºC, by using the same trend observed in the change in density of water as temperature increases.

## 4. Conclusion

The unique bilateral structure of surfactants allows for a variety of interesting applications in society and industry. In this study, we focused on one particular non-ionic surfactant referred to as C10E7P2OH. Six solutions were analyzed by DOSY, T1 and T2 experiments in order to determine the structure and size of the aggregates formed in solution. Three of these solutions contain the surfactant C10E7P2OH in water at concentrations by mass of 2, 3.5 and 5%. Three solutions contain surfactant at identical concentrations, and also D-limonene at 2% by mass.

It was found that the surfactant molecules formed micelles which varied in size according to temperature and concentration. Also, in solutions containing D-limonene, the aggregates were much larger when compared to solutions with equal concentration of surfactant, but which did not contain D-limonene. When combined with the results from DOSY which showed very similar D values for the surfactant and D-limonene molecules in these solutions this indicates that D-limonene incorporates within the surfactant micelles.

Finally, it was determined that for the solutions studied, 2% by mass D-limonene is far too much D-limonene to allow for complete inclusion within the surfactant micelles in solution. The extra D-limonene probably resides in water phase, forming separate aggregates like oil droplets in water, but also evaporating from solution quite readily.

## REFERENCES


1. Gerardino D.; Ortona O.; Paduano L.; Tedeschi A.; Vitagliano V. *Phys. Chem. Chem. Phys;* 2002, 4, 5317-5324.

2. Stubenrauch C.; Nyden M.; Findenegg G.; Lindman B. *Journal of Physical Chemistry*; 1996, 100, 17028-17033.

3. Chesick, John P. *Journal of Chemical Education*; 1989, 66, 283-289.

4. Instruction Manual for *Bruker TOPSPIN 13*

5. Kato H.; Saito T.; Nabeshima M.; Shimada K.; Kinugasa S. *Journal of Magnetic Resonance*; 2006, 180, 266-273.

6. J. Israelachvili, *Thermodynamic and Geometric Aspects of Amphiphile Aggregation into Micelles, Vesicles, and Bilayers, and the Interaction Between Them* In: Corso (Ed.) Physics of Amphiphiles: Micelles, Vesicles, and Microemulsions, Soc. Italiana di Fisica, Bologna, 1985, pp. 24–58

7. Soderman O. et al. *The Interpretation of Nuclear Magnetic Resonance Relaxation Data from Micellar and Microemulsion Systems*.

8. Johnson, R.; Costantino S.; Dorn, H.; Salem, J.; Bethune, D. *Science*; 1992, 255, 1235-1239.

9. Homans, S. W. *A Dictionary of Concepts in NMR*. Oxford University Press, 1992, pg 119.

10. *Surfactants: The ubiquitous Amphiphiles*, http://www.rsc.org/chemistryworld/Issues/2003/July/amphiphiles.asp. 2003.

11. B Lindman; P. Stilbs, *Nuclear Magnetic Resonance of Surfactant Systems* In: Corso (Ed.) Physics of Amphiphiles: Micelles, Vesicles, and Microemulsions, Soc. Italiana di Fisica, Bologna, 1985, pp. 94-121

12. V. Degiorgio, *Nonionic Micelles* In: Corso (Ed.) Physics of Amphiphiles: Micelles, Vesicles, and Microemulsions, Soc. Italiana di Fisica, Bologna, 1985, pp. 303-335

13. C. Leng, *Calculation of Nonionic Ethylene-Oxide Cloud Curves* In: Corso (Ed.) Physics of Amphiphiles: Micelles, Vesicles, and Microemulsions, Soc. Italiana di Fisica, Bologna, 1985, pp. 469-482

14. D Senatra, et al, *Interfacial Polarization, Pyroelectricity and Heat Content in W/O Microemulsions* In: Corso (Ed.) Physics of Amphiphiles: Micelles,

Vesicles, and Microemulsions, Soc. Italiana di Fisica, Bologna, 1985, pp. 802-829

15. Ghosh, S. et al, *Aggregation of Non Ionic Surfactant Igepal in Aqueous Solution: Fluorescence and Light Scattering Studies* In: International Journal of Molecular Sciences; 2003, 4, 562-571.

**Appendix A**

```
/*****************************************************************/
/*      Short Description :                                      */
/*      Program to allow for diffusion measurement in automation */
/*****************************************************************/
/*      Keywords :                                               */
/*      DOSY                    */
/*****************************************************************/
/*      Description/Usage :                                      */
/*      Program to allow diffusion measurements in automation    */
/*      This program stops sample spinning and then calls up the dosy au program */
/*      with parameters for min gradient, max gradient, #experiments, linear or logscale
        */
/*      and starts dosy acquisition     */
/*                                                               */
/*****************************************************************/
/*      Author(s) :                                              */
/*      Name            : Markus Hoffmann, thanks to Kurt Wollenberg
        */
/*      Organisation    : SUNY Brockport        */
/*      Email           : mhoffman@brockport.edu   */
/*****************************************************************/
/*****************************************************************/
/*
$Id: mmhau_dosy, v 1.5 2007/5/15 11:39:39 gsc Exp $
*/
```

| | |
|---|---|
| GETCURDATA | *- Begins automation with designated parameters* |
| STOREPAR("RO",0); | *- Stops the sample from rotating by setting rotation frequency to 0* |
| CPR_exec("sendgui ro acqu",WAIT_TERM); | *- Waits for sample to stop rotating completely* |
| TESET | *- Sets temperature of sample to designated value* |
| TEREADY(300, 0.1); | *- Once temperature is within 0.1 K of set value, waits 300 sec. to proceed* |
| XAU("dosy 10 100 32 l y"); | *- Begins DOSY experiment with settings initial field = 10%, final field = 100%, NS = 32, ramp type = linear* |
| QUIT | *- Ends automation* |